An efficient method for numerical predictions of the performance characteristics of fuel cells. I. Model development and validation

Shiauh-Ping Jung*, Chun-I Lee, Chi-Chang Chen

Green Energy and Environment Research Laboratories, Industrial Technology Research Institute, Hsinchu 31040, Taiwan, ROC

ABSTRACT

This study presents the model development and validation of an efficient method for numerical predictions of the performance characteristics of proton exchange membrane (PEM) fuel cells. To efficiently execute extensive modeling in a short time period, the computational model uses a half-cell at the cathode with only one oxidant channel as the modeling domain. The original three-dimensional (3D) model is replaced with a reduced two-dimensional model. In terms of these computational models and reduced dimensions, mathematical formulations describing physical phenomena within fuel cells are developed. In addition, two-phase Darcy's laws, which are originally only applied to porous media, are further extended to describe the transport and formation of liquid water within channels. In this study, the Fortran programming language is used as a numerical program to implement iterative calculations and predict the overall performance characteristics for three different cases. By comparing the modeling and experimental polarization curves for case 1 and the modeling of points of current density vs. cell voltage (*IV*) of different computational models for cases 2 and 3, this computational model is found to possess a certain degree of accuracy and reliability. In addition, the complete extensive modeling also works more efficiently and with fewer computational resources.

1. Introduction

Although the use of fossil fuels drives economic development and advancement of civilization, the environmental pollution and greenhouse effects accompanying these fuels has encouraged the search for cleaner, more efficient, richer fuels. Hydrogen energy appears to be a viable option. The interest in hydrogen energy has recently led to increasing interest in fuel-cell research and applications. Proton exchange membrane (PEM) fuel cells are particularly widely used with products that have an output power ranging from 1 W to 100 kW because of their high efficiency, low pollution, quietness, and low-temperature start-up characteristics. The future for PEM fuel cells using hydrogen energy is greatly anticipated and is of interest to many people.

Research on PEM fuel cells involves fluid dynamics, heat transfer, electrochemistry, materials, structure analysis, and integration and control of systems. Therefore, harmony and coordination between various technologies is needed to achieve stable and reliable fuel-cell performance. Among these technologies, fuel-cell flow design plays a key role such that modeling research that

utilizes comprehensive computational fluid dynamics (CFD) or simplified numerical analysis has shown great advancements in both quality and quantity. In the 1990s, Springer et al. [1] first presented numerical modeling of PEM fuel cells. Subsequently, Bernardi and Verbrugge [2] and Nguyen and White [3] also developed fuel-cell models. However, during this period, limited computational tools and resources resulted in modeling research focused on one-dimensional (1D) models. In the late 1990s, fuel-cell modeling gradually developed toward two-dimensional (2D) models. At this stage, equations of continuity, momentum, energy, species, current and two-phase flows were used to describe the electrochemistry and transport phenomena within fuel cells. For example, Gurau et al. [4] evaluated polarization curves under various operating conditions with a 2D fuel-cell model and analyzed local variations of properties, such as oxygen and water vapor concentration and current densities. Um et al. [5] investigated the effects of hydrogen dilution on cell performance and polarization with a 2D transient model. It is worth mentioning that the addition of two-phase models further improved the prediction ability of fuel-cell modeling. He et al. [6] used liquid-water transport equations governed by the shear force of gas flows and capillary force to perform simulation and investigation for fuel cells with interdigitated flow fields. Wang et al. [7] analyzed liquid-water transport phenomena within the cathode of fuel cells using a two-phase mixture model [8], in which the effects of flooding on cell performance were evaluated. Since then, research on

* Corresponding author. Current address: 307B, Bldg. 64, 195, Sec. 4, Chung Hsing Rd., Chutung, Hsinchu 31040, Taiwan, ROC. Tel.: +886 3 5832008x137; fax: +886 3 5826239.

E-mail address: jung0066@itri.org.tw (S.-P. Jung).

the 2D, two-phase modeling of fuel cells has been published continually.

By 2000, mainstream research on three-dimensional (3D) fuel-cell modeling, which allowed researchers to understand the physical phenomena and mechanisms within fuel cells more clearly, began to develop. Mazumder and Cole [9,10] performed 3D fuel-cell simulations with gas-phase and two-phase models, respectively. Their work not only evaluated the effects of flooding on cell performance, but also discussed the mechanisms governing liquid-water transport. Hu et al. [11,12] built 3D fuel-cell models with straight and interdigitated channels, in which the cell performances of different channels are compared, and transport phenomena and physical mechanisms for two-phase flows are also analyzed in detail. In addition, the model is especially impressive for large-scale fuel-cell modeling. Meng and Wang [13] built a 3D fuel-cell model with 5-channel serpentine channels using 1 million grids. This was the first time that modeling was realized using the parallel computing methodology. Wang and Wang [14] developed a 50 cm^2 fuel-cell model with 36 channels and used 2.7 million grids to perform simulations of gas-phase flows. Then, Wang and Wang [15] also developed a 200 cm^2 fuel-cell model, in which only gas-phase flows were considered and 23.5 million grids were used in parallel computations. Inoue et al. [16] performed simulations for fuel cells with 225 cm^2 active areas, in which the cell performances of serpentine channels with different channel numbers and patterns are compared. Subsequently, Inoue et al. [16] used their previously developed model [17,18] to evaluate the effects of combinations of different gas and coolant channels on cell performance.

After 2007, the interest in large-scale fuel-cell modeling seems to have declined. Instead, small-scale fuel-cell modeling received more attention. Most of these studies evaluated the effects of flow design on cell performance. For example, Wang et al. [19] investigated how straight and interdigitated channels affect the flooding and cell performances under different operating voltages. Kuo et al. [20] performed fuel-cell simulations with straight and wave channels to analyze microscopic phenomena and compare overall performances. Min [21] presented fuel-cell stepped flow designs, and evaluated the effects of the channel with various step numbers on cell performances. Labato et al. [22] utilized CFD to predict the performances of fuel cells with serpentine, straight, and pin-type channels under different operating conditions, and analyzed how these channel patterns affect the distributions of current densities. In addition, a large number of studies address fuel-cell model developments. For example, Sui et al. [23] built a comprehensive 3D fuel-cell model, and the model was validated based on the comparisons of modeling and experimental results involving fuel cells with straight channels. Ly et al. [24] presented reduced fuel-cell models to decrease the computational requirements and preserve geometrical resolution, and the modeling results are not only consistent with the experimental findings, but these models also reduce the required computational resources and time. Kim et al. [25] developed fuel-cell models with reduced dimensions and compared the modeling results of different dimensional fuel cells with a single straight channel to evaluate which combinations of dimensions possess the best efficiency and accuracy. In addition to the above flow designs and model developments, there has been continual published research about the modeling of fuel-cell operating parameters, cold start and transient response. For example, Yuan et al. [26] utilized CFD to analyze the effects of operating parameters such as the outlet pressure, cell temperature, relative humidity and stoichiometric ratio on cell performances. Jiao and Li [27] performed fuel-cell simulations of various cold start processes and evaluated the ways to reduce water freezing during a cold start. Khajeh-Hosseini-Dalasm et al. [28] developed a two-phase transient model of the fuel-cell cathode side to investigate the time variation of liquid water and gas transport, and good

agreements between modeling and experimental results verified this model.

The decline in large-scale fuel-cell modeling research after 2007 may have occurred because this type of work requires extensive computational resources, and only a few research institutes with access to parallel computing can perform the modeling. It can be determined from the aforementioned previous papers that a simulation for large-scale fuel cells usually requires several hours to several tens of hours, and thus, extensive resources and time must be devoted to conducting modeling research. Although large-scale fuel-cell modeling has received less attention recently for these reasons, this type of research is often so difficult to handle that researchers avoid it as much as possible. The fuel cells used in commercial products are usually large-scale cells. Therefore, in order to solve the above difficulty, this study presents a fuel-cell modeling method programmed in the Fortran computing language that can be applied to PEM fuel cells with various scales. This method can not only predict overall performance characteristics, such as polarization curves, reactant flow rates and pressure drops, but can also provide local property variations to further analyze physical phenomena and mechanisms within fuel cells. The computational models developed in this study are described in detail in the following sections.

2. Model development

In this study, model development covers three sections: computational models, basic assumptions, and mathematical formulations. Each section is discussed separately.

2.1. Computational model

In order to simplify fuel-cell modeling, a cathode physical model that includes only the regions covered by one oxidant channel is considered in this study, as shown in Fig. 1(a) and (b). In Fig. 1(a), the computational domains surrounded by dotted lines in the x–y plane include only active areas, but they may also include active areas and non-active areas, both of which are covered by one oxidant channel and two adjacent half ribs. In Fig. 1(b), a cross-sectional model in the y–z plane is shown that contains one oxidant channel, adjacent ribs, a cathode gas diffusion layer (CGDL), a cathode catalyst layer (CCL), and a half PEM for the domains, including active areas. However, for the domains of non-active areas, only one oxidant channel and adjacent rib are included. A computational model built in this way can not only deal with fuel cells with oxidant channels having straight, serpentine, and Z patterns but can also be applied to large-scale fuel cells while using fewer resources and less time. In the following section, the basic assumptions used in this study are elucidated.

2.2. Basic assumptions

The dimensions considered by this model can be illustrated with Fig. 1(a) and (b). In Fig. 1(a), only the dimension along the direction of oxidant flow is adopted; thus, this model can be regarded as one-dimensional in the x–y plane. In Fig. 1(b), only the dimension along the direction normal to active areas is adopted; hence, this model can be regarded as one-dimensional in the y–z plane. This model consisting of one dimension (along the direction of oxidant flows) plus one dimension (along the z-direction) forms the main framework for developing the following mathematical formulations. The basic assumptions were as follows:

1. Overpotentials within the anode catalyst layer (ACL) are ignored, and only those within the CCL are considered.
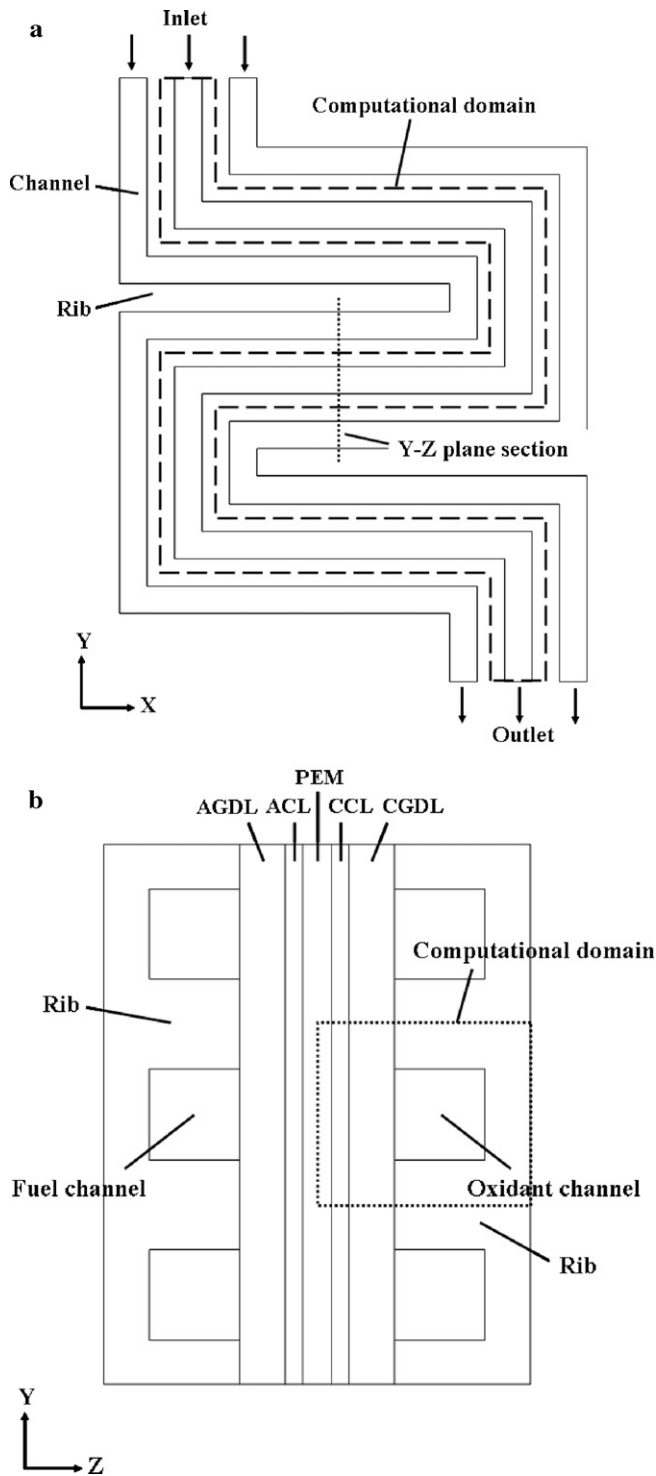
Fig. 1. (a) Fuel-cell computational models in the *x–y* plane. (b) Fuel-cell computational models in the *y–z* plane.

2. According to assumption 1, the electrochemistry and transport phenomena at the anode can be ignored; only those at the cathode are considered.
3. Flow fields at the cathode are steady and laminar.
4. Gas-phase mixtures at the cathode are regarded as ideal gases.
5. Non-uniform distributions of oxidant flows are ignored; thus, the oxidant can be regarded as feeding each channel uniformly.
6. For mass transfer of each gas-phase species, only convection along the streamwise directions within the channels, and only

diffusion along the z-direction within other domains are considered.

7. Only gas-phase pressure variations along streamwise directions within the channels are considered, and gas-phase pressure gradients along the z-direction within other domains are regarded as zero.
8. The temperatures on the rib boundaries are specified, and within other domains, only heat conduction along the z-direction is considered.
9. Only current transfer along the z-direction is considered, and current densities are assumed to be uniform in the z direction.
10. According to assumption 9, both electronic-phase and ionic-phase potential variations only occur in the z-direction.
11. Only liquid-water transport along the streamwise directions within channels and along the z-direction within other domains is considered.
12. Property variations along the direction normal to oxidant flows in the *x–y* plane are ignored; thus, properties are assumed to be constant in this direction.
13. Property variations in the z-direction on PEM boundaries in the vicinity of the anode are ignored; thus, on these boundaries, all property gradients in the z direction are zero.

2.3. Mathematical formulation

2.3.1. Mass conservation of each gas-phase species

$$\frac{\partial n_{i,l}}{\partial l} = \frac{\partial}{\partial z}\left(D_g^i \frac{\partial c_i}{\partial z}\right) + S_c^i \tag{1}$$

$$\frac{d}{dz}\left(D_g^i \frac{dc_i}{dz}\right) + S_c^i = 0 \tag{2}$$

Eqs. (1) and (2) describe mass conservation of each gas-phase species within oxidant channels and other domains, respectively. In these equations, *l* and *z* represent coordinates along the streamwise direction (the direction of oxidant flows) and z-direction, respectively; *i* is the gas-phase species of oxygen, nitrogen, or water vapor; n_{ij} is the gas-phase molar flux along the streamwise direction; D_g^i is the gas-phase diffusivity; c_i is the gas-phase molar density; and S_c^i is the source term of each gas-phase species.

Eqs. (1) and (2) can be simplified by expressing c_i with gas-phase partial pressure as follows:

$$c_i = \frac{P_g^i}{RT} \tag{3}$$

where P_g^i is the gas-phase partial pressure, *R* is the ideal-gas constant, and *T* is the absolute temperature. Substituting Eq. (3) into Eqs. (1) and (2) gives

$$\frac{\partial n_{i,l}}{\partial l} = \frac{\partial}{\partial z}\left[\frac{D_g^i}{R}\frac{\partial}{\partial z}\left(\frac{P_g^i}{T}\right)\right] + S_c^i \tag{4}$$

$$\frac{d}{dz}\left[\frac{D_g^i}{R}\frac{d}{dz}\left(\frac{P_g^i}{T}\right)\right] + S_c^i = 0 \tag{5}$$

In this study, Eqs. (4) and (5) are adopted to describe the mass conservation of each gas-phase species within oxidant channels and other domains, respectively. Using the Bruggeman correction, D_g^i can be expressed as [29] follows:

$$D_g^i = \frac{\varepsilon^\tau (1-s)^\tau (1 - x_g^i)}{\sum\limits_{j,j \neq i} x_g^j / D_g^{ij}} \tag{6}$$

where ε is the porosity, *s* is the liquid saturation, τ is the tortuosity, x_g^i is the gas-phase molar fraction, and D_g^{ij} is the binary diffusivity of

both the i-th and j-th gas-phase species, which can be determined as follows [30]:

$$D_g^{ij} = \frac{10^{-4}a}{P_{i,j}}\left(\frac{T}{\sqrt{T_{ci}T_{cj}}}\right)^b (P_{ci}P_{cj})^{1/3}(T_{ci}T_{cj})^{5/12}(1/M_i + 1/M_j)^{1/2} \quad (7)$$

where a and b are empirical constants and $P_{i,j}$ is the sum of partial pressures of both the i-th and j-th gas-phase species. P_{ci} and P_{cj} are the critical pressures for the i-th and j-th gas-phase species, respectively; T_{ci} and T_{cj} are the critical temperatures for the i-th and j-th gas-phase species, respectively; and M_i and M_j are the molecular weights for the i-th and j-th gas-phase species, respectively. In addition, S_c^i can be expressed as follows:

$$S_c^{O_2} = \begin{cases} \dfrac{-j_T}{4F} & \text{within the CCL} \\ 0 & \text{otherwise} \end{cases} \quad (8)$$

$$S_c^{N_2} = 0 \quad (9)$$

$$S_c^{H_2O} = \begin{cases} \dfrac{-S_s}{M_{H_2O}} & \text{within the channel and CGDL} \\ \dfrac{-S_s}{M_{H_2O}} + \dfrac{\gamma_{H_2O}^{EC}j_T}{2F} + \dfrac{d}{dz}\left(\dfrac{-2.5\lambda}{22}\dfrac{i_z}{F}\right) & \text{within the CCL} \\ \dfrac{-S_s}{M_{H_2O}} + \dfrac{d}{dz}\left(\dfrac{-2.5\lambda}{22}\dfrac{i_z}{F}\right) & \text{within the PEM} \end{cases} \quad (10)$$

Eq. (8) defines the source term of oxygen, $S_c^{O_2}$, where j_T is the volumetric transfer current density, and F is the Faraday constant. It can be determined from Eq. (8) that within the CCL, $S_c^{O_2}$ represents the oxygen consumption rate caused by electrochemical reactions, while within other domains, this term is zero. For $S_c^{N_2}$, because the nitrogen does not participate in electrochemical reactions, it is neither consumed nor generated, which leads to $S_c^{N_2}$ being zero within all domains. Eq. (10) describes the source term of water vapor, $S_c^{H_2O}$, where S_s is the source term of liquid water and thus $-S_s$ is the sink term of water vapor, and M_{H_2O} is the molecular weight of water. $\gamma_{H_2O}^{EC}$ is the correction factor, which indicates the ratio of transport into the cathode to total transport for water vapor produced in electrochemical reactions. In addition, λ is the water content, and i_z is the current density in the z direction.

It can be determined from Eq. (10) that this term $-S_s/M_{H_2O}$ exists within all domains, depending on the phase changes between water vapor and liquid water. Within the CCL, water vapor is produced at the rate of $j_T/2F$ according to electrochemical reactions in which the transport of water vapor toward the anode and cathode is related to the gradient of water-vapor molar density at the anode and cathode, respectively. In order to evaluate the ratio of water-vapor transport toward the cathode gas channel, $\gamma_{H_2O}^{EC}$ can be defined as follows:

$$\gamma_{H_2O}^{EC} = \begin{cases} 0 & \text{for}(dc_{H_2O}/dz)_a = 0 \text{ and } (dc_{H_2O}/dz)_c = 0 \\ \dfrac{-(dc_{H_2O}/dz)_c}{(dc_{H_2O}/dz)_a - (dc_{H_2O}/dz)_c} & \text{otherwise} \end{cases} \quad (11)$$

In Eq. (11), $(dc_{H_2O}/dz)_a$ and $(dc_{H_2O}/dz)_c$ represent the gradients in the z-direction of water-vapor molar density at the anode and cathode, respectively. When $(dc_{H_2O}/dz)_a$ and $(dc_{H_2O}/dz)_c$ are both zero, this represents the fact that water vapor produced by electrochemical reactions neither diffuses from the CCL toward the anode gas channel nor toward the cathode channel, thus leading to $\gamma_{H_2O}^{EC}$ being zero. However, when one of these two terms is not zero, it means that water vapor produced by electrochemical reactions may diffuse from the CCL toward the anode or toward the cathode, where diffusion fluxes toward the anode and cathode are proportional to $(dc_{H_2O}/dz)_a$ and $-(dc_{H_2O}/dz)_c$, respectively. Therefore, $\gamma_{H_2O}^{EC}$ can be

decided by the ratio of $-(dc_{H_2O}/dz)_c$ to $(dc_{H_2O}/dz)_a - (dc_{H_2O}/dz)_c$. The terms $(dc_{H_2O}/dz)_a$ and $(dc_{H_2O}/dz)_c$ can be expressed as follows:

$$\left(\frac{dc_{H_2O}}{dz}\right)_c = \begin{cases} \left[\dfrac{1}{R}\dfrac{d}{dz}\left(\dfrac{P_g^{H_2O}}{T}\right)\right]_c & \text{for} \quad \left[\dfrac{1}{R}\dfrac{d}{dz}\left(\dfrac{P_g^{H_2O}}{T}\right)\right]_c \le 0 \\ 0 & \text{for} \quad \left[\dfrac{1}{R}\dfrac{d}{dz}\left(\dfrac{P_g^{H_2O}}{T}\right)\right]_c > 0 \end{cases} \quad (12)$$

$$\left(\frac{dc_{H_2O}}{dz}\right)_a = \begin{cases} \dfrac{(P_{g,CCL}^{H_2O} - P_{g,ACL}^{H_2O})/RT_{CCL}}{d_{PEM} + (d_{ACL} + d_{CCL})/2} & \text{for} \quad \dfrac{(P_{g,CCL}^{H_2O} - P_{g,ACL}^{H_2O})/RT_{CCL}}{d_{PEM} + (d_{ACL} + d_{CCL})/2} \ge 0 \\ 0 & \text{for} \quad \dfrac{(P_{g,CCL}^{H_2O} - P_{g,ACL}^{H_2O})/RT_{CCL}}{d_{PEM} + (d_{ACL} + d_{CCL})/2} < 0 \end{cases} \quad (13)$$

In Eq. (12), $(dc_{H_2O}/dz)_c$ can be rewritten as $\left[(1/R)d(P_g^{H_2O}/T)/dz\right]_c$ according to $c_{H_2O} = P_g^{H_2O}/(RT)$. When $[(1/R)d(P_g^{H_2O}/T)/dz]_c \le 0$, i.e., water vapor diffuses from the CCL toward the cathode, $(dc_{H_2O}/dz)_c$ is equal to $[(1/R)d(P_g^{H_2O}/T)/dz]_c$. However, when $[(1/R)d(P_g^{H_2O}/T)/dz]_c > 0$, i.e., water vapor diffuses from the cathode toward the CCL, $(dc_{H_2O}/dz)_c$ is forced to be zero, which assumes that it is impossible for water vapor to diffuse from the cathode to the CCL. In Eq. (13), $P_{g,CCL}^{H_2O}$ and $P_{g,ACL}^{H_2O}$ are water-vapor partial pressures within the CCL and ACL, respectively, where $P_{g,CCL}^{H_2O}$ can be obtained from iterative calculations, while $P_{g,ACL}^{H_2O}$ needs to be evaluated in an approximate manner because the electrochemistry and transport phenomena at the anode are ignored. In addition, T_{CCL} is the temperature within the CCL approximated as that within the ACL, and d_{PEM}, d_{ACL}, and d_{CCL} are the thicknesses of the PEM, ACL and CCL, respectively. It can be determined from Eq. (13) that $(dc_{H_2O}/dz)_a$ can be determined by the relation of $(P_{g,CCL}^{H_2O} - P_{g,ACL}^{H_2O})/RT_{CCL}$ divided by $d_{PEM} + (d_{ACL} + d_{CCL})/2$, where $(P_{g,CCL}^{H_2O} - P_{g,ACL}^{H_2O})/RT_{CCL}$ represents the differences between the water-vapor molar density within the CCL and the ACL. When this relation is larger than zero, i.e., water vapor diffuses from the CCL toward the anode, $(dc_{H_2O}/dz)_a$ can be obtained by this relation. However, when this relation is less than zero, $(dc_{H_2O}/dz)_a$ is forced to be zero, which assumes that water-vapor diffusion from the anode to the CCL is impossible. In order to evaluate $P_{g,ACL}^{H_2O}$, an approximate method is adopted, as follows.

First, the water-vapor partial pressure at the anode inlet, $P_{g,in,a}^{H_2O}$, can be calculated as follows:

$$P_{g,in,a}^{H_2O} = RH_{in}^a P_{sat}^{in,a} \quad (14)$$

where RH_{in}^a and $P_{sat}^{in,a}$ are relative humidity and saturation pressure at the anode inlet, respectively. According to ideal-gas laws, the hydrogen molar flow rate at the anode inlet, $N_{H_2}^{in,a}$, can be expressed as follows:

$$N_{H_2}^{in,a} = \frac{(P_{g,in,a}^{total} - P_{g,in,a}^{H_2O})Q_a^{in}}{RT_a^{in}} \quad (15)$$

In Eq. (15), the gas-phase total pressure at the anode inlet, $P_{g,in,a}^{total}$ is approximated as that at the anode outlet, $P_{g,out,a}^{total}$, and T_a^{in} is the temperature at the anode inlet. Therefore, substituting the known values $N_{H_2}^{in,a}$, $P_{g,in,a}^{total}$, T_a^{in} and $P_{g,in,a}^{H_2O}$ into Eq. (15) gives the gas-phase volumetric flow rate at the anode inlet, Q_a^{in}. After obtaining Q_a^{in}, according to ideal-gas laws, water-vapor molar flow rates at the anode inlet and outlet, i.e., $N_{H_2O}^{in,a}$ and $N_{H_2O}^{out,a}$, can be expressed as follows:

$$N_{H_2O}^{out,a} \approx N_{H_2O}^{in,a} = \frac{P_{g,in,a}^{H_2O} Q_a^{in}}{RT_a^{in}} \quad (16)$$

In Eq. (16), $N_{H_2O}^{out,a}$ is approximated as $N_{H_2O}^{in,a}$, which assumes that water-vapor molar flow rates within the fuel channel are constant.

The hydrogen molar flow rate at the anode outlet, $N_{H_2}^{out,a}$, can be expressed as follows:

$$N_{H_2}^{out,a} = N_{H_2}^{in,a} - \frac{I}{2F} \tag{17}$$

where I is the output current, and thus $I/2F$ stands for the total consumption rate of hydrogen in power generation.

With Eqs. (15)–(17), the water-vapor partial pressure at the anode outlet, $P_{g,out,a}^{H_2O}$, can be calculated as follows:

$$P_{g,out,a}^{H_2O} = \frac{P_{g,out,a}^{total} N_{H_2O}^{out,a}}{N_{H_2}^{out,a} + N_{H_2O}^{out,a}} \tag{18}$$

After obtaining $P_{g,in,a}^{H_2O}$ and $P_{g,out,a}^{H_2O}$, $P_{g,ACL}^{H_2O}$ can be evaluated using linear interpolation between $P_{g,in,a}^{H_2O}$ and $P_{g,out,a}^{H_2O}$ as follows:

$$P_{g,ACL}^{H_2O} = \begin{cases} P_{g,in,a}^{H_2O} + \frac{L_p}{L_t}(P_{g,out,a}^{H_2O} - P_{g,in,a}^{H_2O}) \text{ for } \text{ parallel } \text{ flow} \\ P_{g,out,a}^{H_2O} + \frac{L_p}{L_t}(P_{g,in,a}^{H_2O} - P_{g,out,a}^{H_2O}) \text{ for } \text{ counter } \text{ flow} \end{cases} \tag{19}$$

where L_p is the partial length from the inlet to the corresponding computational grids of the oxidant channel and L_t is the total length of the oxidant channel. When the flows of fuel and oxidant are parallel, the first term in Eq. (19) is used to evaluate $P_{g,ACL}^{H_2O}$, and when flows of fuel and oxidant are counter to one another, the second term in Eq. (19) is used.

In addition, it can be determined from Eq. (10) that within the CCL and PEM, water-vapor transport driven by proton drags $d[(-2.5\lambda/22)(i_z/F)]/dz$ also needs to be considered [1]. This term describes how when protons move with the rate of i_z/F from the ACL to the CCL, water vapor dragged by these ions can also move together with them, where the number of water molecules carried by one proton is equal to $2.5\lambda/22$. λ is further defined below.

2.3.2. Gas-phase momentum conservation

$$\frac{dP_g}{dl} = -\frac{f_g}{D}\frac{\rho_g V_{g,l}^2}{2} - \frac{K_{L,g}}{\delta l}\frac{\rho_g V_{g,l}^2}{2} + \rho_g g \cos\theta_{l/g} \tag{20}$$

Eq. (20) describes gas-phase momentum conservation within the oxidant channel, where P_g is the gas-phase pressure, l is the coordinate along the streamwise direction, f_g is the gas-phase friction factor, and D is the channel hydraulic diameter. ρ_g is the gas-phase density, $V_{g,l}$ is the gas-phase velocity along the streamwise direction, $K_{L,g}$ is the gas-phase local resistance, and δl is the local channel length. In addition, g is the gravitational acceleration, and $\theta_{l/g}$ is the included angle of oxidant flows relative to gravity, where $\theta_{l/g} = 0°$ and $\theta_{l/g} = 180°$ represent the fact that oxidant flows are parallel and counter to gravity, respectively, while $\theta_{l/g} = 90°$ represents the fact that oxidant flows cannot be affected by gravity. D can be expressed as follows:

$$D = \frac{2w_C d_C}{w_C + d_C} \tag{21}$$

where w_c is the channel width and d_c is the channel depth.

$V_{g,l}$ can be determined as follows:

$$V_{g,l} = \frac{n_{g,l} RT}{P_g} \tag{22}$$

where $n_{g,l}$ is the gas-phase molar flux along the steamwise direction and can be expressed with the sum of molar fluxes of each gas-phase species as follows:

$$n_{g,l} = \sum_i^N n_{i,l} \tag{23}$$

ρ_g can be expressed as follows:

$$\rho_g = \frac{\sum_i^N n_{i,l} M_i}{V_{g,l}} \tag{24}$$

where $\sum_i^N n_{i,l} M_i$ is the sum of mass fluxes of each gas-phase species.

f_g can be expressed as [31] follows:

$$f_g = \left[55 + 41.5\exp\left(\frac{-3.4}{w/d}\right)\right]\frac{1}{Re_g k_{rg}} \tag{25}$$

where Re_g is the gas-phase Reynolds number and k_{rg} is the gas-phase relative permeability. Re_g can be defined as follows:

$$Re_g = \frac{\rho_g V_{g,l} D}{\mu_g} \tag{26}$$

where μ_g is the gas-phase dynamic viscosity and can be determined as follows [30]:

$$\mu_g = \sum_i^N \frac{x_g^i \mu_g^i}{\sum_j x_g^j \Phi_g^{ij}} \tag{27}$$

$$\Phi_g^{ij} = \frac{1}{\sqrt{8}}\left(1 + \frac{M_i}{M_j}\right)^{-1/2}\left[1 + \left(\frac{\mu_g^i}{\mu_g^j}\right)^{1/2}\left(\frac{M_j}{M_i}\right)^{1/4}\right]^2 \tag{28}$$

where μ_g^i and μ_g^j are the dynamic viscosities of the i-th and j-th gas-phase species, respectively, which can be calculated according to Sutherland's law as follows:

$$\mu_g^i = \frac{A_i T^{1.5}}{B_i + T} \tag{29}$$

where A_i and B_i both are empirical constants, and T is the absolute temperature.

κ_{rg} can be expressed as [32,33] follows:

$$\kappa_{rg} = (1-s)^3 \tag{30}$$

It can be determined from Eq. (30) that when s is zero (i.e., there is an absence of liquid water within the channel), k_{rg} is one, while when s is not zero (i.e., the presence of liquid water within the channel), κ_{rg} decreases with increasing s. Therefore, combining Eqs. (25) and (30) shows that f_g can increase with increasing s, which means that stronger flooding can lead to greater gas-phase flow resistance produced within the channel.

$K_{L,g}$ can be expressed as [34] follows:

$$K_{L,g} = \begin{cases} 0 & \text{for } \text{straight } \text{channel } \text{sections} \\ \frac{L_e}{D}f_g & \text{for } \text{channel } \text{bends} \end{cases} \tag{31}$$

It can be determined from Eq. (31) that $K_{L,g}$ is zero for straight channel sections, while $K_{L,g}$ can be written as the product of L_e/D and f_g for channel bends, where L_e/D is the dimensionless equivalent length depending on the relative radius of channel bends.

2.3.3. Energy conservation

$$\frac{d}{dz}\left(k_{eff}\frac{dT}{dz}\right) + S_T = 0 \tag{32}$$

Eq. (32) describes heat conduction in the z-direction within the fuel cell, where k_{eff} is the effective thermal conductivity and S_T is the heat source. k_{eff} can be expressed as [29] follows:

$$k_{eff} = -2k_s + \frac{1}{\varepsilon/(2k_s + k_{f,mix}) + 1 - \varepsilon/(3k_s)} \tag{33}$$

where k_s and $k_{f,mix}$ are the thermal conductivities of solids and fluids, respectively, and $k_{f,mix}$ can be defined as follows:

$$k_{f,mix} = sk_l + (1-s)k_g \tag{34}$$

where k_l and k_g are the thermal conductivities of liquid phases and gas phases, respectively, and k_g can be defined as [30] follows:

$$k_g = \sum_i^N \frac{x_g^i k_g^i}{\sum_j x_g^j \Phi_g^{ij}} \tag{35}$$

$$\Phi_g^{ij} = \frac{1}{\sqrt{8}} \left(1 + \frac{M_i}{M_j} \right)^{-1/2} \left[1 + \left(\frac{k_g^i}{k_g^j} \right)^{1/2} \left(\frac{M_g^j}{M_g^i} \right)^{1/4} \right]^2 \tag{36}$$

where k_g^i and k_g^j are the thermal conductivities of the i-th and j-th gas-phase species, respectively, which can be determined according to the Eucken formula [30] as follows:

$$k_g^i = \left(C_{p,g}^i + \frac{5}{4} \frac{R}{M_i} \right) \mu_g^i \tag{37}$$

where $C_{p,g}^i$ is the constant-pressure specific heat of the i-th gas-phase species and can be determined according to the Jannaf method as follows:

$$C_{p,g}^i = \frac{R}{M_i} \left(a_1^i + a_2^i T + a_3^i T^2 + a_4^i T^3 + a_5^i T^4 \right) \tag{38}$$

where $a_1^i - a_5^i$ are empirical constants and T is the absolute temperature.

S_T can be expressed as follows:

$$S_T = \begin{cases} -i_z \dfrac{d\phi_s}{dz} & \text{within the rib and CGDL} \\[2mm] -i_z \dfrac{d\phi_s}{dz} + j_T \eta & \text{within the CCL} \\[2mm] -i_z \dfrac{d\phi_f}{dz} & \text{within the PEM} \end{cases} \tag{39}$$

where ϕ_s and ϕ_f are electronic-phase and ionic-phase potentials, respectively, and η is the overpotential. It can be determined from Eq. (39) that heat sources within both the rib and the CGDL are Joule heating equal to the product of i_z and $-d\phi_s/dz$, which represents the conversion from electric energy to heat energy caused by electric-phase resistivity. The heat source within the CCL includes not only the Joule heating but also the irreversible heat source, $j_T\eta$, which represents the waste heat produced in the process of conversion from chemical energy to electric energy. Heat sources within the PEM are the Joule heating equal to the product of i_z and $-d\phi_f/dz$, which represents the conversion from electric energy to heat energy caused by ionic resistivity.

Interfacial temperature changes resulting from contact thermal resistance between the rib and CGDL can be calculated as follows:

$$\delta T = R_T^{rib/GDL}(i_z \delta\phi_s^{rib/GDL}) \tag{40}$$

where δT is the interfacial temperature change, $R_T^{rib/GDL}$ is the contact thermal resistance of the rib/CGDL interfaces, and $\delta\phi_s^{rib/GDL}$ is the interfacial change of the electric-phase electric potentials caused by $R_T^{rib/GDL}$.

2.3.4. Open-circuit voltages and polarization losses

Open-circuit voltages can be expressed as [31] follows:

$$V_{oc}^C = 1.482 - 0.000845T + 0.0000431T \ln[P_g^{H_2}(P_g^{O_2})^{0.5}] \tag{41}$$

Eq. (41) defines the open-circuit voltage within the CCL, V_{oc}^C, where T is the absolute temperature and $P_g^{H_2}$ and $P_g^{O_2}$ are the hydrogen partial pressure within the ACL and the oxygen partial pressure

within the CCL, respectively. $P_g^{O_2}$ can be obtained from iterative computations, but $P_g^{H_2}$ needs to be evaluated using Eq. (19) and $P_{g,ACL}^{H_2} = P_{g,out,a}^{total} - P_{g,ACL}^{H_2O}$. The open-circuit voltage within the ACL, V_{oc}^A, is assumed to be zero.

Overpotentials can be determined according to the following equations [6,31]:

$$i_z = (1-s)i_0^{ref} \left(\frac{P_g^{O_2}}{P_g^{ref}} \right)^{0.5} \exp\left[-\frac{E_C}{RT} \left(1 - \frac{T}{T_{ref}} \right) \right]$$
$$\times \left[\exp\left(\frac{\alpha F\eta_c}{RT} \right) - \exp\left(\frac{-\alpha F\eta_c}{RT} \right) \right] \tag{42}$$

where i_z is the current density in the z-direction, $(1-s)$ represents the ratio of effective catalyst surface area to total catalyst surface area, i_0^{ref} is the reference transfer current density, $P_g^{O_2}$ is the oxygen partial pressure, P_g^{ref} is the reference pressure, and E_c is the activation energy for oxygen reduction on Pt. T_{ref} is the reference temperature, α is the transfer coefficient, and η_c is the cathode overpotential. i_z can be calculated with Eq. (42), and i_z/d_{CCL} gives j_T because j_T can be approximated as the gradient of i_z in the z direction, i.e., $j_T = di_z/dz$. During iterative computations, in order to solve η_c, another expression equivalent to Eq. (42) needs to be used:

$$\eta_c = \frac{RT}{\alpha F} \log\left[\frac{i_z}{2i_{0,z}} + \left(\frac{i_z^2}{4i_{0,z}^2} + 1 \right)^{0.5} \right] \tag{43}$$

η_c determined with Eq. (43) is positive, where $i_{0,z}$ is the surface transfer current density and can be expressed as follows:

$$i_{0,z} = (1-s)i_0^{ref} \left(\frac{P_g^{O_2}}{P_g^{ref}} \right)^{0.5} \exp\left[-\frac{E_C}{RT} \left(1 - \frac{T}{T_{ref}} \right) \right] \tag{44}$$

Ionic-phase ohmic losses, $\delta\phi_f$, can be calculated as follows:

$$\delta\phi_f = \frac{i_z d_f}{\bar{\sigma}_f} \tag{45}$$

$\delta\phi_f$ determined with Eq. (45) is positive, where d_f is the effective thickness equal to $d_{PEM} + (d_{ACL} + d_{CCL})/2$. $\bar{\sigma}_f$ is the ionic conductivity and is defined as the average of σ_f^{ACL} and σ_f^{CCL}, i.e., $\bar{\sigma}_f = (\sigma_f^{ACL} + \sigma_f^{CCL})/2$. σ_f at the anode or cathode can be expressed as [1] follows:

$$\sigma_f = (0.5139\lambda - 0.326)\exp\left[1268\left(\frac{1}{303} - \frac{1}{T} \right) \right] \tag{46}$$

$$\lambda = \begin{cases} 0.043 + 17.18a - 39.85a^2 + 36.0a^3 & 0 < a \le 1 \\ 14 + 1.4(a-1) & 1 < a \le 3 \\ 16.8 & a > 3 \end{cases} \tag{47}$$

$$a = \frac{P_g^{H_2O}}{P_{sat}} \tag{48}$$

$$P_{sat} = e^{-5800.2206T^{-1} + 1.3914993 - 0.048640239T + 0.41764768 \times 10^{-4}T^2 - 0.14452093 \times 10^{-7}T^3 + 6.5459673 \ln T} \tag{49}$$

It can be determined from Eq. (46) that σ_f is a function of water content, λ and absolute temperature, T. Eq. (47) shows that λ depends on water activity, a, which is related to water-vapor partial pressure, $P_g^{H_2O}$ and saturation pressure, P_{sat}, as shown in Eq. (48), where P_{sat} can be calculated using Eq. (49) [31]. When Eqs. (46)–(49) are used to determine σ_f^{CCL}, all of the necessary properties can be obtained from iterative computations. However, for ionic conductivity within the ACL, $P_{g,ACL}^{H_2O}$ from Eq. (19) and T, approximated as the temperature within the CCL, are substituted into Eqs. (46)–(49) to evaluate σ_f^{ACL}.

Electronic-phase ohmic losses, $\delta\phi_s$ can be expressed as follows:

$$\delta\phi_s = i_z R_{s,z} \tag{50}$$

$\delta\phi_s$ determined from Eq. (50) is positive, where $R_{s,z}$ is the effective electric resistivity in the z-direction of the bipolar plate or GDL, or the effective contact electric resistance in the z-direction between the rib and GDL, which can be expressed as [31] follows:

$$R_{s,z}^{BP} = \left(\frac{w_L + w_C}{w_L} d_C + \frac{d_{BP}}{2} \right) R_{BP,z} + \frac{(w_L + w_C) w_C}{4 d_{BP}} R_{BP,xy} \tag{51}$$

$$R_{s,z}^{GDL} = d_{GDL} R_{GDL,z} + \frac{(w_L + w_C) w_C}{8 d_{GDL}} R_{GDL,xy} \tag{52}$$

$$R_{s,z}^{CR} = \frac{w_L + w_C}{w_L} R_{CR}^{rib/GDL} \tag{53}$$

Eqs. (51) and (52) define the effective electric resistivity of the bipolar plate and GDL, $R_{s,z}^{BP}$ and $R_{s,z}^{GDL}$, respectively, and Eq. (53) defines the effective contact electric resistance of rib/GDL interfaces, $R_{s,z}^{CR}$. In these equations, w_L is the rib width between gas channels or coolant channels, w_C is the width of gas channels or coolant channels, d_C is the depth of gas channels or coolant channels, d_{BP} is the thickness of the bipolar plate minus the sum of the depth of gas channels plus that of coolant channels, and d_{GDL} is the GDL thickness. $R_{BP,z}$ and $R_{BP,xy}$ are the electric resistivity of the bipolar plate in the z and x–y directions, and $R_{CR}^{rib/GDL}$ is the contact electric resistance of rib/GDL interfaces.

For the bipolar plate with one surface containing gas channels and another one containing coolant channels, $R_{s,z}^{BP}$ needs to be evaluated for the gas and coolant side, respectively, while for the bipolar plate with only one surface containing gas channels, $R_{s,z}^{BP}$ needs to be evaluated only for the gas side. To calculate the electronic-phase ohmic losses of a single cell, Eqs. (51)–(53) are first used to evaluate $R_{s,z}^{BP}$, $R_{s,z}^{GDL}$ and $R_{s,z}^{CR}$ at the anode and cathode, respectively. Then, Eq. (50) is applied to both the anode and cathode to obtain $\delta\phi_s$. However, in this study, because only current densities at the cathode side are available, electronic-phase ohmic losses at the anode or coolant side are evaluated by substituting the average current densities into Eq. (50). In addition, it can be determined from Eqs. (51)–(53) that effective electric resistivity depends not only on the properties of the component itself, but also the effects of geometry parameters on current transfer. For example, the bipolar plate with wider and deeper channels can yield greater $R_{s,z}^{BP}$, and when the GDL is thicker or the gas channel is wider, $R_{s,z}^{GDL}$ becomes larger. $R_{CR}^{rib/GDL}$ can increase with increasing ratios of the channel width to rib width, w_c/w_L.

2.3.5. Computations of local cell voltages

In order to compute local cell voltages, this study presents an equation capable of describing how local cell voltages are related to the open-circuit voltage and various polarization losses. Fig. 2 illustrates the variations of electronic-phase and ionic-phase potentials within the cell. It can be determined from Fig. 2 that the electronic-phase potential at the anode boundary is ϕ_s^A, and the electronic-phase ohmic loss at the anode is $\delta\phi_s^A$, thus leading to the electronic-phase potential within the ACL, ϕ_s^{ACL}, which is equal to $\phi_s^A - \delta\phi_s^A$. The correlation between the open-circuit voltage, overpotential and both electronic-phase and ionic-phase potentials within the ACL can be expressed as follows:

$$-\eta_A = \phi_s^{ACL} - \phi_f^{ACL} - V_{oc}^A \tag{54}$$

where η_A is the anode overpotential, assumed to be zero, ϕ_f^{ACL} is the ionic-phase potential within the ACL, and V_{oc}^A is the open-circuit voltage within the ACL, and its value is zero. Therefore, it can be determined from Eq. (54) that ϕ_s^{ACL} is equal to ϕ_f^{ACL}. The correlation
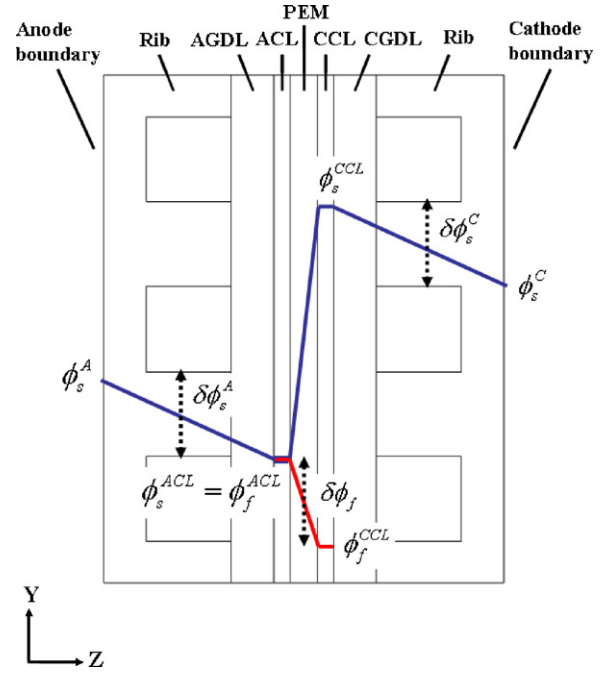

Fig. 2. Variations of electronic-phase and ionic-phase potentials within the fuel cell.

of ionic-phase potentials between the ACL and CCL can be expressed as follows:

$$\phi_f^{CCL} = \phi_f^{ACL} - \delta\phi_f \tag{55}$$

where ϕ_f^{CCL} is the ionic-phase potential within the CCL and $\delta\phi_f$ is the ionic-phase ohmic loss between the ACL and CCL. The correlation between the open-circuit voltage, overpotential and both electronic-phase and ionic-phase potentials within the CCL can also be expressed in a manner similar to Eq. (54):

$$-\eta_C = \phi_s^{CCL} - \phi_f^{CCL} - V_{oc}^C \tag{56}$$

where η_C is the cathode overpotential and ϕ_f^{CCL} is the ionic-phase potential within the CCL. Combining Eqs. (54)–(56) yields ϕ_s^{CCL}:

$$\phi_s^{CCL} = V_{oc}^C + \phi_s^A - \delta\phi_s^A - \delta\phi_f - \eta_C \tag{57}$$

After obtaining ϕ_s^{CCL}, the electronic-phase potential at the cathode boundary can be written as follows:

$$\phi_s^C = \phi_s^{CCL} - \delta\phi_s^C \tag{58}$$

where ϕ_s^C is the electronic-phase potential at the cathode boundary and $\delta\phi_s^C$ is the electronic-phase ohmic loss at the cathode. Therefore, the local cell voltage, $\phi_s^C - \phi_s^A$, can be expressed as follows:

$$\phi_s^C - \phi_s^A = V_{oc}^C - \eta_C - \delta\phi_s - \delta\phi_f \tag{59}$$

where $\delta\phi_s$ is the sum of the electronic-phase ohmic losses at the anode and cathode, i.e., $\delta\phi_s = \delta\phi_s^A + \delta\phi_s^C$. It can be determined from Eq. (59) that the local cell voltage is equal to the open-circuit voltage minus all polarization losses. According to Eq. (59), the local cell voltage can be obtained by evaluating V_{oc}^C, η_C, $\delta\phi_s$ and $\delta\phi_f$, respectively. Compared with solving potential equations with the Laplace form, this study uses simple algebraic operations in place of complicated differential equations, thus numerical computations can be further simplified.

2.3.6. Liquid-water transport and production

In order to simulate two-phase flows within the fuel cell, the two-phase Darcy's law [32], originally only applied to porous media, is further developed into mathematical formulations that

can describe liquid-water transport and production not only within porous media but also within the oxidant channel. By solving related governing equations, liquid saturation is obtained so that the effects of flooding on the local phenomena and the overall performance of fuel cells can be evaluated. According to Darcy's law for two-phase flow, liquid-phase momentum conservation within the oxidant channel can be expressed as follows:

$$\frac{dP_l}{dl} = -\frac{\nu_l \rho_l V_{l,l}}{K_p^e k_{rl}} + \rho_l g \cos \theta_{l/g} \tag{60}$$

where P_l is the liquid-phase pressure, l is the coordinate along the streamwise direction, ν_l is the liquid-phase kinematic viscosity, and K_p^e is the equivalent absolute permeability of the channel. $\rho_l V_{l,l}$ is the liquid-phase mass flux along the streamwise direction, where ρ_l is the liquid-phase density, and $V_{l,l}$ is the liquid-phase velocity along the streamwise direction. k_{rl} is the liquid-phase relative permeability, which can be determined according to $k_{rl} = s^3$ [33], and g_l is the component in the l direction of gravitational acceleration. P_l can be expressed with the gas-phase pressure, P_g, and the capillary pressure, P_c, as [32]:

$$P_l = P_g - P_c \tag{61}$$

where P_c can be determined as follows [35]:

$$P_c = \sigma \cos \theta_c \left(\frac{\varepsilon}{K_p^e}\right)^{1/2} J(s) \tag{62}$$

$$J(s) = \begin{cases} 1.417(1-s) - 2.120(1-s)^2 + 1.263(1-s)^3, & \text{if } \theta_C < 90° \\ 1.417s - 2.120s^2 + 1.263s^3, & \text{if } \theta_C > 90° \end{cases} \tag{63}$$

In Eq. (62), σ is the surface tension, θ_C is the contact angle, ε is the porosity, and $J(s)$ is the Leverett J-function, as shown in Eq. (63). Combining Eqs. (60)–(63) and rearranging yields governing equations with the variable s.

For the hydrophilic channel of $\theta_C < 90°$:

$$\sigma \cos \theta_c \left(\frac{\varepsilon}{K_p^e}\right)^{1/2} s^3 \left[-1.417 + 4.240(1-s) - 3.789(1-s)^2\right] \frac{ds}{dl}$$
$$= s^3 \frac{dP_g}{dl} + \frac{\nu_l \rho_l V_{l,l}}{K_p} - s^3 \rho_l g \cos \theta_{l/g} \tag{64}$$

For the hydrophobic channel of $\theta_C > 90°$:

$$\sigma \cos \theta_c \left(\frac{\varepsilon}{K_p^e}\right)^{1/2} s^3 \left(1.417 - 4.240s + 3.789s^2\right) \frac{ds}{dl}$$
$$= s^3 \frac{dP_g}{dl} + \frac{\nu_l \rho_l V_{l,l}}{K_p} - s^3 \rho_l g \cos \theta_{l/g} \tag{65}$$

For porous media, only liquid-water transport in the z-direction is considered and the gas-phase pressure gradient in the z-direction, dP_g/dz is ignored. Therefore, the related governing equations can be obtained by substituting the z coordinate for the l coordinate and taking dP_g/dz as zero.

For hydrophilic porous media of $\theta_C < 90°$:

$$\sigma \cos \theta_c \left(\frac{\varepsilon}{K_p}\right)^{1/2} s^3[-1.417 + 4.240(1-s) - 3.789(1-s)^2]\frac{ds}{dz}$$
$$= \frac{\nu_l \rho_l V_{l,z}}{K_p} - s^3 \rho_l g \cos \theta_{z/g} \tag{66}$$

For hydrophobic porous media of $\theta_C < 90°$:

$$\sigma \cos \theta_c \left(\frac{\varepsilon}{K_p}\right)^{1/2} s^3 \left(1.417 - 4.240s + 3.789s^2\right) \frac{ds}{dz}$$
$$= \frac{\nu_l \rho_l V_{l,z}}{K_p} - s^3 \rho_l g \cos \theta_{z/g} \tag{67}$$

where K_p is the absolute permeability of porous media, $\rho_l V_{l,z}$ is the liquid-phase mass flux in the z-direction, where $V_{l,z}$ is the liquid-phase velocity in the z-direction, and $\theta_{z/g}$ is the included angle of liquid flows relative to the gravity within porous media. ($\theta_{z/g} = 0°$ and $\theta_{z/g} = 180°$ represent the fact that liquid flows are parallel and counter to gravity, respectively, while $\theta_{z/g} = 90°$ represents the fact that liquid flows cannot be affected by gravity.)

In order to calculate K_p^e in Eqs. (64) and (65), first, Eq. (60) can be rewritten in a manner similar to Eq. (20) as follows:

$$\frac{dP_l}{dl} = -\frac{f_l}{D} \frac{\rho_l V_{l,l}^2}{2} - \frac{K_{L,l}}{\delta l} \frac{\rho_l V_{l,l}^2}{2} + \rho_l g \cos \theta_{l/g} \tag{68}$$

where the friction factor, f_l can be expressed as follows:

$$f_l = \left[55 + 41.5 \exp\left(\frac{-3.4}{w_C/d_C}\right)\right] \frac{1}{Re_l k_{rl}} \tag{69}$$

The liquid-phase Reynolds number, Re_l, can be expressed as follows:

$$Re_l = \frac{\rho_l V_{l,l} D}{\mu_l} \tag{70}$$

The liquid-phase local resistance, $K_{L,l}$, can be expressed as follows:

$$K_{L,l} = \begin{cases} 0 & \text{for channel straight sections} \\ \frac{L_e}{D} f_l & \text{for channel bends} \end{cases} \tag{71}$$

Substituting Eqs. (69)–(71) into Eq. (68) gives

$$\frac{dP_l}{dl} = -\frac{[55 + 41.5 \exp(-3.4/(w_C/d_C))](1 + r_{K_L} D/\delta l)}{2D^2} \frac{\nu_l \rho_l V_{l,l}}{k_{rl}}$$
$$+ \rho_l g \cos \theta_{l/g} \tag{72}$$

Then, by comparing equivalent Eqs. (60) and (72), K_p^e can be determined as follows:

$$K_p^e = \frac{2D^2}{\left[55 + 41.5 \exp(-3.4/(w_C/d_C))\right] (1 + (r_{K_L} D/\delta l))} \tag{73}$$

$$r_{K_L} = \begin{cases} 0 & \text{for channel straight sections} \\ L_e/D & \text{for channel bend} \end{cases} \tag{74}$$

It can be determined from Eqs. (73) and (74) that the K_p^e of straight channel sections depends on both D and w_C/d_C, while the K_p^e of channel bends is related to L_e/D as well as D and w_C/d_C. Therefore, it may be predicted that compared with straight channel sections, a smaller K_p^e is formed for channel bends, and this can lead to apparent differences of flooding within the channel.

In Eqs. (64)–(67), $\rho_l V_{l,l}$ and $\rho_l V_{l,z}$ are variables that both need to be solved and can be determined as follows:

$$\frac{\partial \rho_l V_{l,l}}{\partial l} = -\frac{\partial \rho_l V_{l,z}}{\partial z} + S_s \tag{75}$$

$$\frac{d\rho_l V_{l,z}}{dz} = S_s \tag{76}$$

$$S_s = \begin{cases} M_{H_2O} k_c \frac{\varepsilon(1-s)x_g^{H_2O}}{RT}(P_g^{H_2O} - P_{sat}) & \text{if } P_g^{H_2O} > P_{sat} \\ M_{H_2O} k_e \frac{\varepsilon(1-s)s\rho_l}{M_{H_2O}}(P_g^{H_2O} - P_{sat}) & \text{if } P_g^{H_2O} < P_{sat} \end{cases} \tag{77}$$

Eq. (75) describes liquid-phase mass conservation within the oxidant channel, in which the liquid-phase mass flow rate per unit

volume along the streamwise direction, $d\rho_l V_{l,l}/dl$, is equal to the sum of the liquid-phase mass flow rate per unit volume in the z-direction, $-d\rho_l V_{l,z}/dz$, and the liquid-phase source within the channel, S_s. Eq. (76) describes liquid-phase conservation within porous media, where the liquid-phase mass flow rate per unit volume in the z-direction, $d\rho_l V_l/dz$, is equal to the liquid-phase source therein, S_s. S_s can be determined using Eq. (77), where the first and second terms represent the liquid-phase source and sink, respectively, both of which result from phase changes between water vapor and liquid water. In addition, k_c and k_e are the condensation and evaporation constant, respectively, and $x_g^{H_2O}$ is the water-vapor molar fraction. It can be determined from Eq. (77) that when the water-vapor pressure, $P_g^{H_2O}$, is larger than the saturation pressure, P_{sat}, S_s represents the condensation rate from water vapor to liquid water, while when $P_g^{H_2O}$ is smaller than P_{sat}, S_s represents the evaporation rate from liquid water to water vapor.

3. Results and discussion

To verify the accuracy and reliability of the computational models developed in this study, three cases were analyzed in sequence to perform a systematic evaluation and examination. Original fuel-cell models for each case and the simplified ones adopted by this study are shown in Fig. 3(a)–(c), respectively, and detailed physical parameters and operating conditions are tabulated in Table 1. In these cases, case 1 is the fuel-cell experiment presented by Ticianelli et al. [36], and cases 2 and 3 are fuel-cell simulations presented by Wang and Wang [14,15]. Although these studies give detailed operating conditions, they cannot provide all of the physical parameters necessary for the present computational models. For unavailable physical parameters, this study assumes reasonable values to define them. The operating conditions and physical parameters for these cases are discussed further in the following paragraphs.
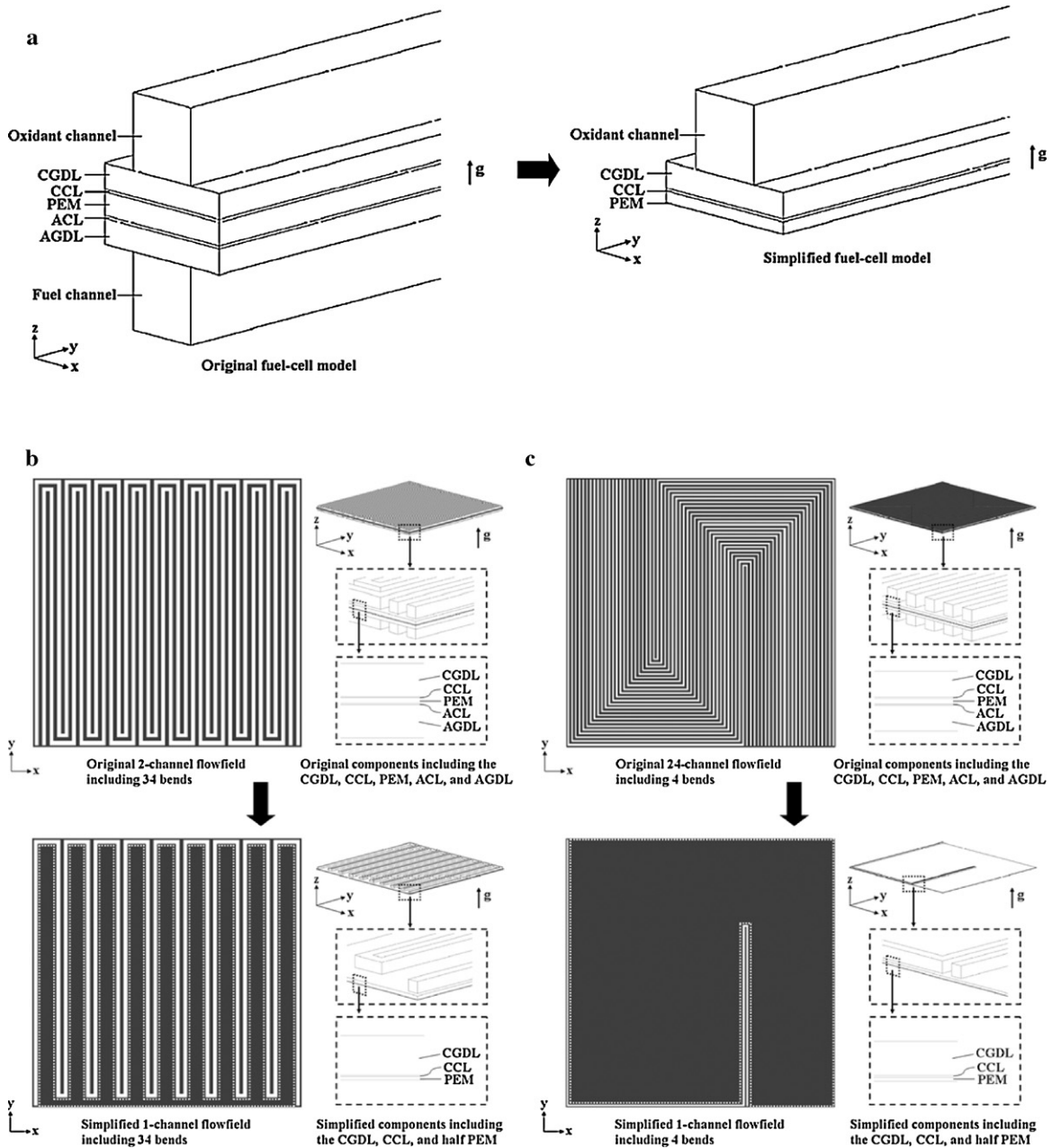

Fig. 3. (a) Original fuel-cell models and simplified ones for case 1. (b) Original fuel-cell models and simplified ones for case 2. (c) Original fuel-cell models and simplified ones for case 3.

Table 1
Physical parameters and operating conditions for each case.

Quantity	Case 1	Case 2	Case 3
Gas channel pattern	Straight pattern	Serpentine pattern	Serpentine pattern
Gas channel length, L_t^{gas}	71.12 mm	1299 mm	431 mm
Gas channel depth, d_C^{gas}	0.762 mm	1.0 mm	1.0 mm
Gas channel width, w_C^{gas}	0.762 mm	1.0 mm	1.0 mm
Shoulder width between gas channels, w_L^{gas}	0.762 mm	1.0 mm	1.0 mm
Coolant channel pattern	NA	NA	Serpentine pattern
Coolant channel length, $L_t^{coolant}$	NA	NA	431 mm
Coolant channel depth, $d_C^{coolant}$	NA	NA	1.0 mm
Coolant channel width, $w_C^{coolant}$	NA	NA	1.0 mm
Shoulder width between coolant channels, $w_L^{coolant}$	NA	NA	1.0 mm
BP thickness, d_{BP}	2.286 mm	3.0 mm	3.0 mm
BP electrical resistivity in x–y direction, $R_{BP,xy}$	5×10^{-5} Ω m	5×10^{-5} Ω m	5×10^{-5} Ω m
BP electrical resistivity in z direction, $R_{BP,z}$	24×10^{-5} Ω m	24×10^{-5} Ω m	24×10^{-5} Ω m
BP thermal conductivity, k_s^{BP}	20 W m^{-1} k^{-1}	20 W m^{-1} k^{-1}	20 W m^{-1} k^{-1}
BP contact angle, θ_c^{BP}	80°	80°	80°
GDL thickness, d_{GDl}	0.254 mm	0.3 mm	0.2 mm
GDL porosity, ε_{GDL}	0.4	0.6	0.6
GDL tortuosity, τ_{GDL}	1.5	1.5	1.5
GDL permeability, K_P^{GDL}	1.76×10^{-11} m^2	10^{-12} m^2	10^{-12} m^2
GDL electrical resistivity in x–y direction, $R_{GDL,xy}$	0	0	0
GDL electrical resistivity in z direction, $R_{GDL,z}$	5.77×10^{-5} Ω m	5.77×10^{-5} Ω m	5.77×10^{-5} Ω m
GDL thermal conductivity, k_s^{GDL}	1.7 W m^{-1} k^{-1}	1.7 W m^{-1} k^{-1}	1.7 W m^{-1} k^{-1}
GDL contact angle, θ_c^{GDL}	100°	100°	100°
CL thickness, d_{CL}	0.0287 mm	0.01 mm	0.01 mm
CL porosity, ε_{CL}	0.4	0.4	0.4
PEM thickness, d_{PEM}	0.23 mm	0.051 mm	0.045 mm
PEM porosity, ε_{PEM}	0.28	0.28	0.28
Contact electrical resistance between the rib and GDL, $R_{CR}^{rib/GDL}$	0	0	0
Contact thermal resistance between the rib and GDL, $R_T^{rib/GDL}$	0	0	0
Dimensionless equivalent length, Le/D	0	60	60
Density of liquid water, ρ_l	977.8 kg m^{-3}		
Kinematic viscosity of liquid water, v_l	4.14×10^{-7} m^2 s^{-1}		
Thermal conductivity of liquid water, k_l	0.66 W m^{-1} k^{-1}		
Surface tension, σ	0.0625 N m^{-1}		
Gravity, g	9.8 m s^{-2}		
Molecular weight of N$_2$, M_{N_2}	28 g mol^{-1}		
Molecular weight of O$_2$, M_{O_2}	32 g mol^{-1}		
Molecular weight of H$_2$O, M_{H_2O}	18 g mol^{-1}		
Experimental constant, a for N$_2$ and O$_2$/H$_2$O	$2.745 \times 10^{-4}/3.640 \times 10^{-4}$		
Experimental constant, b for N$_2$ and O$_2$/H$_2$O	1.823/2.334		
Critical pressure, p_{ci} for N$_2$/O$_2$/H$_2$O	33.5/49.7/221.2 atm		
Critical temperature, T_{ci} for N$_2$/O$_2$/H$_2$O	126.2/154.4/647.3 K		
Experimental constant, A_i for N$_2$/O$_2$/H$_2$O	$1.405 \times 10^{-6}/1.783 \times 10^{-6}/1.867 \times 10^{-6}$ kg s^{-1} m^{-1} K$^{-0.5}$		
Experimental constant, B_i for N$_2$/O$_2$/H$_2$O	111.5/156/708 K		
Experimental constant, a_1^i for N$_2$/O$_2$/H$_2$O	3.298677/3.212936/3.386842		
Experimental constant, a_2^i for N$_2$/O$_2$/H$_2$O	$1.40824 \times 10^{-3}/1.127486 \times 10^{-3}/3.474982 \times 10^{-3}$ K^{-1}		
Experimental constant, a_3^i for N$_2$/O$_2$/H$_2$O	$-3.963222 \times 10^{-6}/-5.75615 \times 10^{-7}/-6.354696 \times 10^{-6}$ K^{-2}		
Experimental constant, a_4^i for N$_2$/O$_2$/H$_2$O	$5.641515 \times 10^{-9}/1.313877 \times 10^{-9}/6.968581 \times 10^{-9}$ K^{-3}		
Experimental constant, a_5^i for N$_2$/O$_2$/H$_2$O	$-2.444855 \times 10^{-12}/-8.768554 \times 10^{-13}/-2.506588 \times 10^{-12}$ K^{-4}		
Universal ideal gas constant, R	8.3145 kJ kmol^{-1} K^{-1}		
Faraday constant, F	96,485 C mol^{-1}		
Condensation rate constant, k_c	100 s^{-1}		
Evaporation rate constant, k_e	1 atm^{-1} s^{-1}		
Reference pressure, P_g^{ref}	101,325 Pa		
Activation energy, E_C	66 kJ mol^{-1}		
Reference temperature, T_{ref}	298.15 K		
Transfer coefficient, α	0.5		
Cathode reference exchange current density, i_0^{ref}	0.15 A m^{-2}	0.20 A m^{-2}	0.20 A m^{-2}
Fuel/oxidant	H$_2$/air	H$_2$/air	H$_2$/air
Anode/cathode inlet flow rate, $N_{H_2}^{in,a}/N_{O_2}^{in,c}$	$2.8 \times 10^4/3.0 \times 10^4$ A m^{-2} equivalent	$i_z^{avg} \leq 10^3$ A m^{-2}: $2.0 \times 10^3/2.0 \times 10^3$ A m^{-2} equivalent $i_z^{avg} > 10^3$ A m^{-2}: 2.0/2.0 stoichiometric	$i_z^{avg} \leq 10^3$ A m^{-2}: $2.0 \times 10^3/2.0 \times 10^3$ A m^{-2} equivalent $i_z^{avg} > 10^3$ A m^{-2}: 2.0/2.0 stoichiometric
Anode/cathode inlet temperature, T_a^{in}/T_c^{in}	50/50 °C; 80/80 °C	80/80 °C	80/80 °C

Table 1 (*Continued*)

Quantity	Case 1	Case 2	Case 3
Anode/cathode inlet relative humidity, RH_{in}^a/RH_{in}^c	100%/100%	100%/0%	50%/50%
Anode/cathode outlet pressure, $P_{g,out,a}^{total}/P_{g,out,c}^{total}$	1.0/1.0 atm; 3.0/5.0 atm	2.0/2.0 atm	2.0/2.0 atm
Fuel cell temperature, T_{cell}	50 °C; 80 °C	80 °C	80 °C; 72–82 °C with the oxidant flow

First, in case 1, experimental polarization curves were measured with fixed reactant flow rates, where the anode and cathode inlet flow rates, $N_{H_2}^{in,a}$ and $N_{O_2}^{in,c}$, are equivalent to those generating current densities of 2.8×10^4 and 3.0×10^4 A m^{-2}, respectively, and the oxidant and fuel flows are parallel. Under fixed flow rates, three different operating conditions were used, where the anode/cathode inlet temperature and the outlet pressure are 50/50 °C and 1.0/1.0 atm, 50/50 °C and 3.0/5.0 atm, and 80/80 °C and 3.0/5.0 atm, respectively. In this study, these three operating conditions are represented as case 1(a), case 1(b) and case 1(c), respectively, for convenience. In the experiments by Ticianelli et al. [36], how the fuel cell is oriented relative to gravity is unknown. In order to obtain $\theta_{l/g}$ and $\theta_{z/g}$, which are necessary for the computational models, it is assumed that fluid flows within the oxidant channel cannot be affected by gravity, while fluid flows within the CGDL are parallel to gravity. Therefore, $\theta_{l/g}$ and $\theta_{z/g}$ are specified as 90° and 0°, respectively. In addition, for predictions of polarization curves of case 1, this study chooses 13 operating points, including 10, 20, 50, and 100–1000 mA cm^{-2} with an interval of 100 mA cm^{-2}, to simulate cell voltages corresponding to specific current densities. From the simulation of case 1 performed in this study, the predicted and experimental polarization curves are compared to evaluate whether computational models can yield qualitative and quantitative agreement with experiments under different operating conditions.

In case 2, a 3D fuel-cell model, which includes the reactant flow fields of the anode and cathode, was built by Wang and Wang [14], and in case 3, a 3D fuel-cell model that includes the reactant flow fields of the anode and cathode and the coolant flow fields was built by Wang and Wang [15]. For cases 2 and 3, the active areas are 50 and 200 cm^2, respectively, and the flow fields are a two-channel serpentine pattern with a channel length of 1299 mm and a 24-channel serpentine pattern with a channel length of 431 mm, respectively. Case 2 is simulated numerically for cell voltages of 0.65 V under specific operating conditions, and case 3 for current densities of 1 A cm^{-2} under two different cell temperatures, which are a constant 80 °C and an increasing 72–82 °C with oxidant flows, respectively. Therefore, the predictions of Wang and Wang [14,15] include only a single point of current density vs. cell voltage (IV); therefore, no polarization curves are available for comparison. In addition, the reactant flow rates of both cases are given with stoichiometric feeding, where $N_{H_2}^{in,a}$ and $N_{O_2}^{in,c}$ are equivalent to stoichiometric flow rates of 2.0 and 2.0, respectively. However, in this study, two-step flow rates are used to simultaneously satisfy reactant feeding for the simulated points of Wang and Wang [14,15] and stability and convergence in numerical computations. That is, when the average current density, i_z^{avg}, is inferior or equal to 10^3 A m^{-2}, $N_{H_2}^{in,a}$ and $N_{O_2}^{in,c}$ are both equivalent to flow rates generating current densities of 2.0×10^3 A m^{-2}, while when i_z^{avg} is greater than 10^3 A m^{-2}, $N_{H_2}^{in,a}$ and $N_{O_2}^{in,c}$ are equivalent to stoichiometric flow rates of 2.0 and 2.0, respectively.

In the research of Wang and Wang [14,15], it is also unknown how the fuel cell is oriented relative to gravity. Therefore, $\theta_{l/g}$ and $\theta_{z/g}$ are similarly specified as 90° and 0°, respectively, to give the physical parameters necessary for cases 2 and 3. For predictions

of the polarization curves of cases 2 and 3, this study chooses 18 operating points, including 10, 20, 50, and 100–1500 mA cm^{-2} with an interval of 100 mA cm^{-2}, to simulate cell voltages corresponding to specific current densities. In case 3, simulations under a constant 80 °C or an increasing 72–82 °C with oxidant flows are represented as case 3(a) and case 3(b), respectively. The simulations of cases 2 and 3 performed in this study are focused on evaluating whether computational models can predict overall performance characteristics, such as polarization curves, reactant flow rates and pressure drops, in an efficient manner and capture the IV points predicted by Wang and Wang [14,15]. Therefore, the computational resources and the time required between this study and Wang and Wang [14,15] will also be compared. The results and discussion are divided into five sections, which are comparisons between experiments and predictions for case 1, predicted open-circuit voltages and polarization losses of case 1, the predicted overall performance of case 2, the predicted overall performance of case 3, and comparisons of modeling ability between different computational models.

3.1. Comparisons between experiments and predictions for case 1

Figs. 4–6 show the comparisons between experiments and predictions for case 1 under different operating conditions. It can be determined by observing the overall polarization curves from Figs. 4–6 that numerical predictions indeed can capture experimental data varying with different operating conditions, both qualitatively and quantitatively. First, for case 1(a), with operating conditions of 50/50 °C and 1.0/1.0 atm, the experimental and predicted IV values vary from 1.000 V at 0 mA cm^{-2} and 1.201 V at 0 mA cm^{-2} to 0.050 V at 1000 mA cm^{-2} and 0.331 V at 1000 mA cm^{-2}, respectively. Then, for case 1(b), with operating conditions of 50/50 °C and 3.0/5.0 atm, experimental and predicted IV values vary from 1.020 V at 0 mA cm^{-2} and 1.228 V at 0 mA cm^{-2} to 0.350 V at 1000 mA cm^{-2} and 0.413 V at 1000 mA cm^{-2}, respectively. Finally, for case 1(c) with operating conditions of 80/80 °C and 3.0/5.0 atm, experimental and predicted IV values vary from
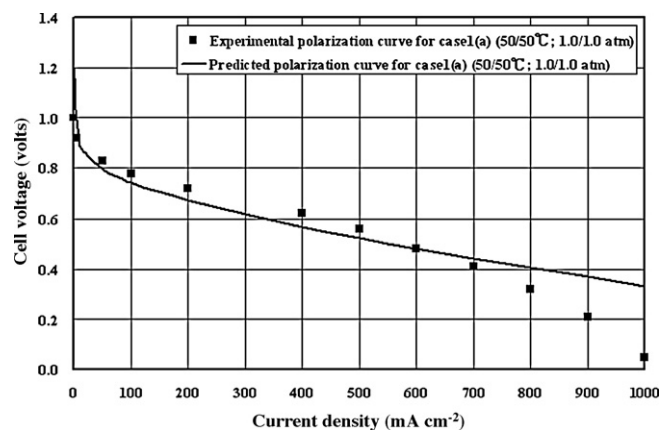

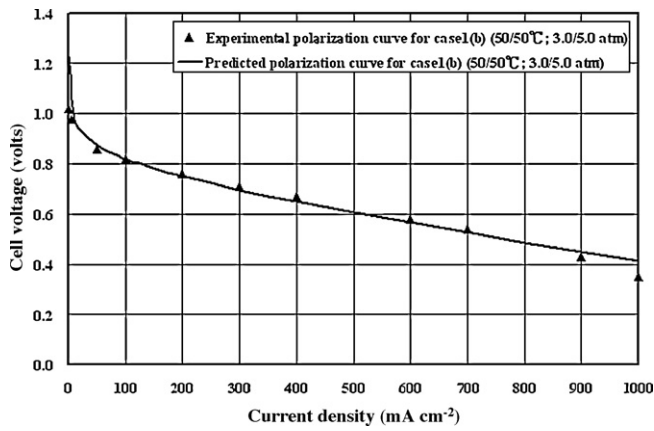**Fig. 4.** Comparisons between experiments and predictions for case 1(a).

Fig. 5. Comparisons between experiments and predictions for case 1(b).
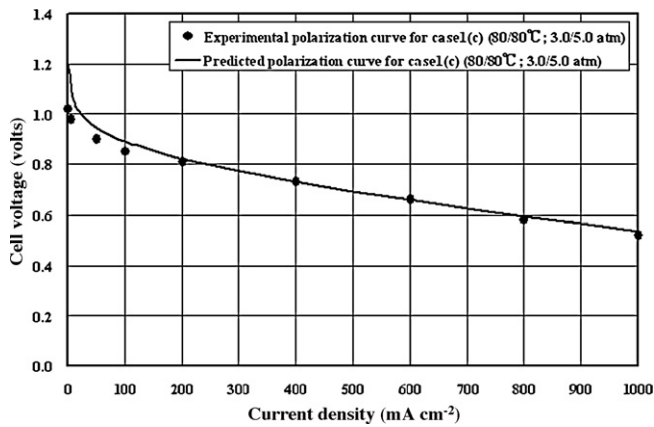

Fig. 6. Comparisons between experiments and predictions for case 1(c).
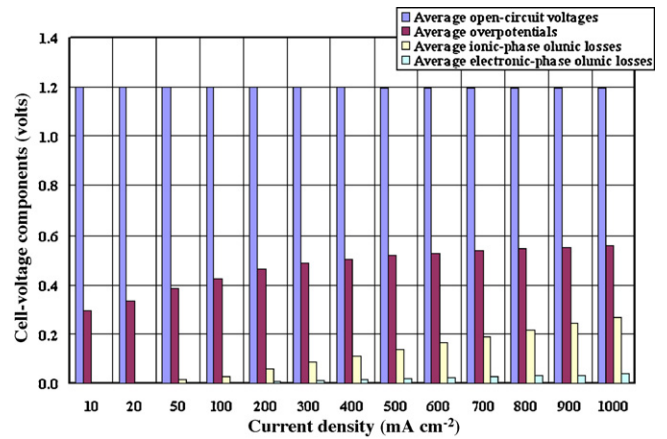

Fig. 7. Predicted open-circuit voltages and polarization losses for case 1(a).

Fig. 8. Predicted open-circuit voltages and polarization losses for case 1(b).

1.020 V at 0 mA cm^{-2} and 1.204 V at 0 mA cm^{-2} to 0.520 V at 1000 mA cm^{-2} and 0.535 V at 1000 mA cm^{-2}, respectively.

Further comparisons of the experimental and predicted IV values for case 1(a) reveal that the predicted cell voltages underestimate the experimental data for low current densities between 0 and 200 mA cm^{-2} and intermediate current densities between 200 and 600 mA cm^{-2}, while they overestimate the experimental data for high current densities between 600 and 1000 mA cm^{-2}. For case 1(b), the predicted cell voltages fit the experimental data for low current densities between 0 and 200 mA cm^{-2} and intermediate current densities between 200 and 600 mA cm^{-2}, while they overestimate the experimental data for high current densities between 600 and 1000 mA cm^{-2}. For case 1(c), the predicted cell voltages overestimate the experimental data for low current densities between 0 and 200 mA cm^{-2}, while they fit the experimental data for intermediate current densities between 200 and 600 mA cm^{-2} and high current densities between 600 and 1000 mA cm^{-2}.

The reasons for the differences between the experiments and the predictions may include the fact that computational models cannot describe physical phenomena precisely and the fact that the operating conditions cannot be controlled accurately; hence, the computational models use incorrect parameters. Although Ticianelli et al. [36] provided only one set of experimental parameters and no detailed flow rates and cell temperatures under different current densities, the computational models developed by this study can still predict the changing trends of polarization curves corresponding to experiments under different operating conditions. Therefore, from the comparisons between predictions and experiments for case 1, the accuracy and reliability of the computational models is demonstrated. In order to investigate the effects of open-circuit voltages and polarization losses on cell voltages, as shown in Eq. (59), the various components forming cell voltages are described and analyzed.
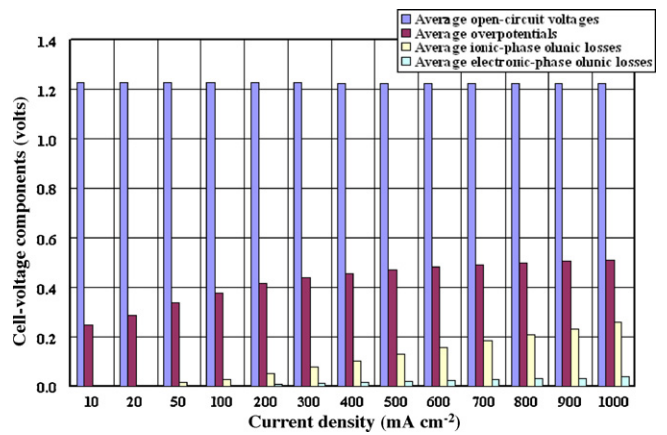
3.2. Predicted open-circuit voltages and polarization losses for case 1

Figs. 7–9 show predicted open-circuit voltages and polarization losses under different operating conditions for case 1, where the

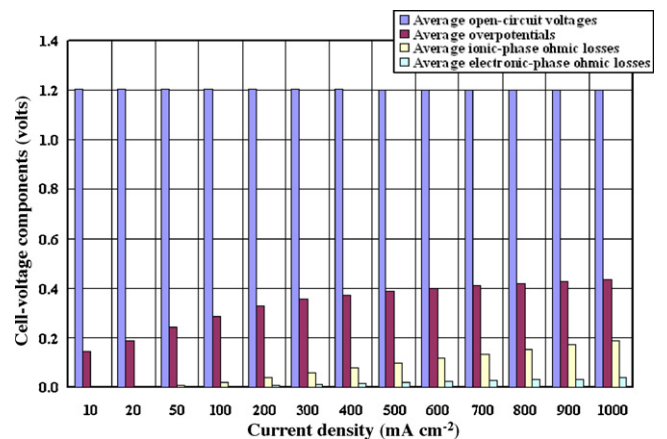Fig. 9. Predicted open-circuit voltages and polarization losses for case 1(c).

x-axis represents the current density, and the *y*-axis represents the various components that constitute the cell voltages. These components contain average open-circuit voltages, $\bar{V}_{oc}^C$, average overpotentials, $\bar{\eta}_C$, average ionic-phase ohmic losses, $\overline{\delta\phi_f}$, and average electronic-phase ohmic losses, $\overline{\delta\phi_s}$. It can be determined from Eq. (59) that cell voltages $\phi_s^C - \phi_s^A$ can be expressed as $V_{oc}^C - \eta_C - \delta\phi_s - \delta\phi_f$, and thus average cell voltages $\overline{\phi_s^C - \phi_s^A}$ can be expressed as $\bar{V}_{oc}^C - \bar{\eta}_C - \overline{\delta\phi_s} - \overline{\delta\phi_f}$. According to $\overline{\phi_s^C - \phi_s^A} = \bar{V}_{oc}^C - \bar{\eta}_C - \overline{\delta\phi_s} - \overline{\delta\phi_f}$, variations of average cell voltages with increasing current densities under different operating conditions can be explained by analyzing each component of the cell voltage.

First, it can be determined from observing $\bar{V}_{oc}^C$ in respective figures that when current densities increase, $\bar{V}_{oc}^C$ varies little. Comparing $\bar{V}_{oc}^C$ under the same current densities, it is found that $\bar{V}_{oc}^C$ increases with increasing anode and cathode outlet pressures. That is, $\bar{V}_{oc}^C$ increases from 1.201 V at 10 mA cm^{-2}–1.196 V at 1000 mA cm^{-2} in Fig. 7 to 1.229 V at 10 mA cm^{-2}–1.224 V at 1000 mA cm^{-2} in Fig. 8. However, when cell temperatures increase, $\bar{V}_{oc}^C$ decreases instead, where $\bar{V}_{oc}^C$ decreases from the values shown in Fig. 8 to 1.204 V at 10 mA cm^{-2}–1.200 V at 1000 mA cm^{-2} in Fig. 9. Then, by observing $\bar{\eta}_C$, it is determined that this value increases with increasing current densities. By comparing $\bar{\eta}_C$ under the same current densities, it is determined that $\bar{\eta}_C$ decreases with increasing anode and cathode outlet pressures and cell temperatures. That is, $\bar{\eta}_C$ decreases from 0.295 V at 10 mA cm^{-2}–0.560 V at 1000 mA cm^{-2} in Fig. 7 to 0.248 V at 10 mA cm^{-2}–0.512 V at 1000 mA cm^{-2} in Fig. 8, and then to 0.147 V at 10 mA cm^{-2}–0.436 V at 1000 mA cm^{-2} in Fig. 9.

Additionally, it is observed that $\overline{\delta\phi_f}$ increases with increasing current densities. When comparing $\overline{\delta\phi_f}$ under the same current densities, it can be determined that $\overline{\delta\phi_f}$ decreases with increasing anode and cathode outlet pressures and cell temperatures. That is, $\overline{\delta\phi_f}$ decreases from 0.003 V at 10 mA cm^{-2}–0.266 V at 1000 mA cm^{-2} in Fig. 7 to 0.003 V at 10 mA cm^{-2}–0.259 V at 1000 mA cm^{-2} in Fig. 8, and then to 0.002 V at 10 mA cm^{-2}–0.189 V at 1000 mA cm^{-2} in Fig. 9. Finally, observations reveal that $\overline{\delta\phi_s}$ increases with increasing current densities. By comparing $\overline{\delta\phi_s}$ under the same current densities, it can be determined that $\overline{\delta\phi_s}$ is consistent; the values of $\overline{\delta\phi_s}$ in Figs. 7–9 all vary from 4×10^{-4} V at 10 mA cm^{-2} to 0.039 V at 1000 mA cm^{-2}.

Based on the above description for case 1, overpotentials are the primary polarization losses, ionic-phase ohmic losses are the secondary, and electronic-phase ohmic losses are the minimum. However, when operating conditions change, the variability in open-circuit voltages and polarization losses also changes. To explain these phenomena, the properties governing open-circuit voltages and polarization losses need to be identified first so that the interactions between various components of cell voltages and governing properties can be further understood. The distributions of governing properties will be presented in the second part of this series of studies to analyze and discuss the effects of these properties on various components of cell voltages in depth.

3.3. Modeling results of overall performance characteristics for case 2

Figs. 10–12 show the comparisons of predicted *IV* values and output powers between different computational models, predicted oxidant flow rates and pressure drops, and predicted open-circuit voltages and polarization losses, respectively, for case 2. Fig. 10 shows that the *IV* values predicted by the computational models of this study vary from 1.191 V at 0 mA cm^{-2} to 0.536 V at 1500 mA cm^{-2} and that the predicted powers vary from 0 W at 0 mA cm^{-2} to 40.2 W at 1500 mA cm^{-2}. For a cell voltage of 0.64 V,
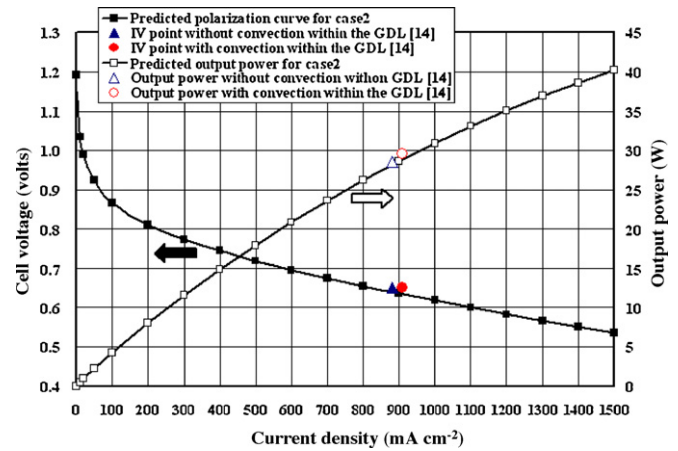

Fig. 10. Comparisons of predicted *IV* values and output powers between different computational models for case 2.
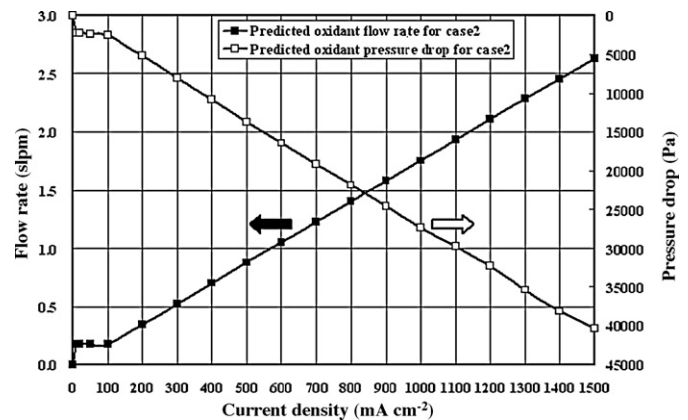

Fig. 11. Predicted oxidant flow rates and pressure drops for case 2.

the predicted current density and the power are 900 mA cm^{-2} and 28.8 W, respectively. For simulations at a cell voltage of 0.65 V, performed by Wang and Wang [14], considering and ignoring convection effects within GDLs can result in different current densities and output powers, which are 880 mA cm^{-2} and 28.6 W, and 910 mA cm^{-2} and 29.6 W, respectively. Therefore, compared with the predictions of Wang and Wang [14], the computational models of this study can not only accurately reproduce the current density and output power at specific cell voltage, but can also quickly give predictions at other cell voltages to produce polarization curves and
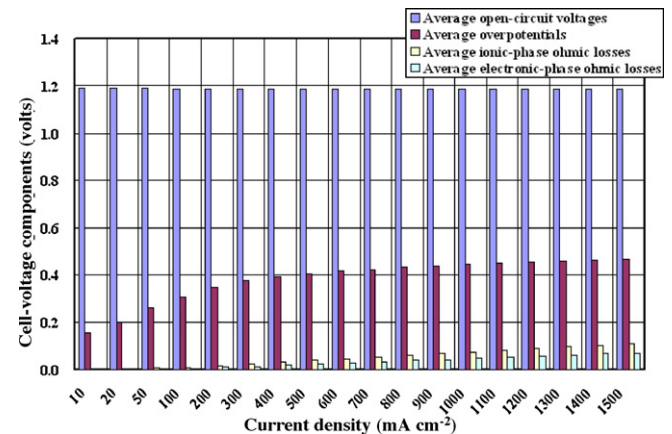

Fig. 12. Predicted open-circuit voltages and polarization losses for case 2.
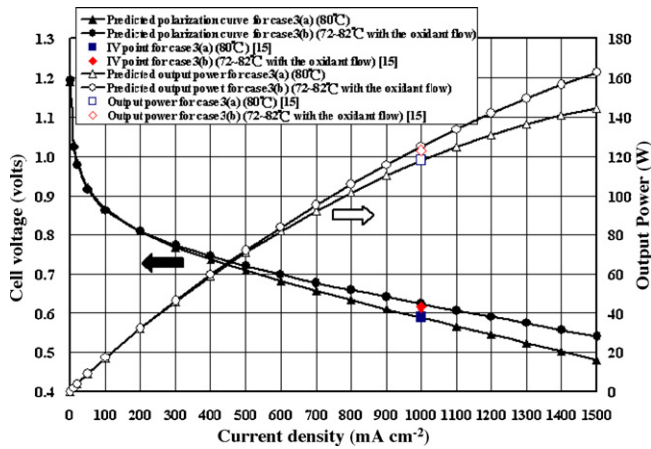
Fig. 13. Comparisons of predicted *IV* values and output powers between different computational models for case 3.

corresponding powers, which are not available from the original research [14].

Fig. 11 shows that the predicted oxidant flow rates vary from 0 slpm at 0 mA cm^{-2} to 2.633 slpm at 1500 mA cm^{-2} and that the predicted pressure drops vary from 0 Pa at 0 mA cm^{-2} to 40,264 Pa at 1500 mA cm^{-2}. At a current density of 900 mA cm^{-2}, the predicted oxidant flow rates and pressure drops are 1.580 slpm and 24,630 Pa, respectively. Finally, it can be determined from Fig. 12 that when current densities increase, $\bar{V}_{oc}^{C}$ varies little with the value ranging between 1.191 V at 10 mA cm^{-2} and 1.183 V at 1500 mA cm^{-2}, while $\bar{\eta}_{C}$, $\overline{\delta\phi}_{f}$ and $\overline{\delta\phi}_{s}$ all increase. By comparing various polarization losses, it is found that that $\bar{\eta}_{C}$ is the primary loss, with a value ranging between 0.154 V at 10 mA cm^{-2} and 0.466 V at 1500 mA cm^{-2}; $\overline{\delta\phi}_{f}$ is the secondary loss, with a value ranging between 0.001 V at 10 mA cm^{-2} and 0.110 V at 1500 mA cm^{-2}; and $\overline{\delta\phi}_{s}$ is the minimum loss, with a value ranging between 5×10^{-4} V at 10 mA cm^{-2} and 0.070 V at 1500 mA cm^{-2}.

3.4. Modeling results of overall performance characteristics for case 3

Figs. 13–16 show the comparisons of predicted *IV* values and output powers between different computational models, predicted oxidant flow rates and pressure drops, and predicted open-circuit voltages and polarization losses, respectively, for case 3. Fig. 13 shows that for case 3(a), with a cell temperature of a constant 80 °C, the *IV* values predicted by the computational models in this
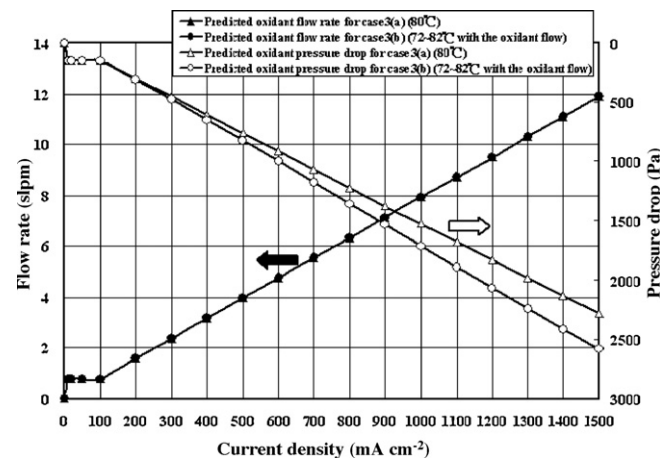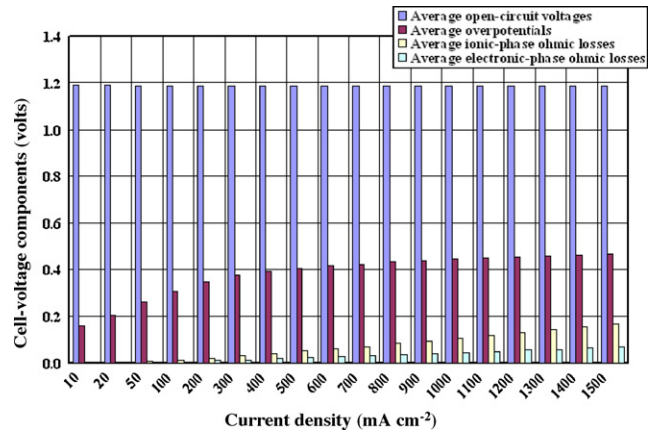
study vary from 1.190 V at 0 mA cm^{-2} to 0.481 V at 1500 mA cm^{-2}. The predicted powers vary from 0 W at 0 mA cm^{-2} to 144.3 W at 1500 mA cm^{-2}, where at a current density of 1000 mA cm^{-2}, the predicted cell voltage and power are 0.590 V and 118.0 W, respectively. For case 3(b), with a cell temperature increasing with oxidant flows from 72 to 82 °C, the predicted *IV* values vary from 1.193 V at 0 mA cm^{-2} to 0.542 V at 1500 mA cm^{-2}. The predicted powers vary from 0 W at 0 mA cm^{-2} to 162.6 W at 1500 mA cm^{-2}, where at a current density of 1000 mA cm^{-2}, the predicted cell voltage and power are 0.624 V and 124.8 W, respectively. In simulations for a current density of 1000 mA cm^{-2} performed by Wang and Wang [15], case 3(a) and case 3(b) can result in different cell voltages and output powers, which are 0.590 V and 118.0 W and 0.616 V and 123.2 W, respectively. For case 3, the computational models in this study can not only reproduce cell voltage and output power at a specific current density, but can also predict polarization curves and corresponding powers that cannot be achieved by the model developed in the original research [15].

Fig. 14 shows that for case 3(a) and case 3(b), the predicted oxidant flow rates vary from 0 slpm at 0 mA cm^{-2} to 11.884 slpm at 1500 mA cm^{-2} and from 0 slpm at 0 mA cm^{-2} to 11.882 slpm at 1500 mA cm^{-2}, respectively. Furthermore, the predicted pressure drops vary from 0 Pa at 0 mA cm^{-2} to 2280 Pa at 1500 mA cm^{-2} and from 0 Pa at 0 mA cm^{-2} to 2583 Pa at 1500 mA cm^{-2}, respectively. In addition, at a current density of 1000 mA cm^{-2}, the predicted oxidant flow rate and pressure drop are 7.926 slpm and 1528 Pa, respectively, for case 3(a) and 7.925 slpm and 1714 Pa, respectively, for case 3(b). Finally, it can be determined from Figs. 15 and 16
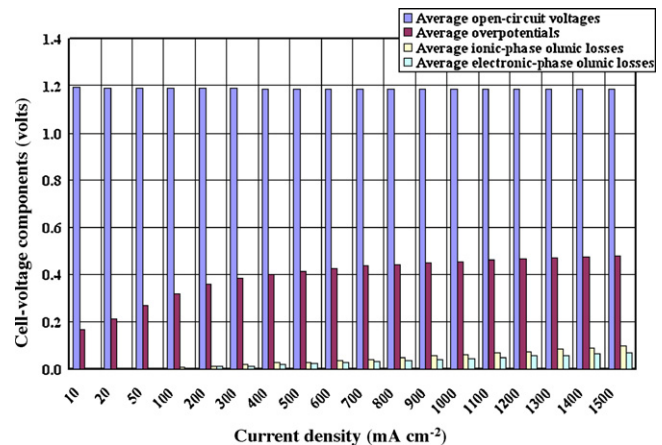

Fig. 15. Predicted open-circuit voltages and polarization losses for case 3(a).

Fig. 14. Predicted oxidant flow rates and pressure drops for case 3.

Fig. 16. Predicted open-circuit voltages and polarization losses for case 3(b).

Table 2
Comparisons of computational resources and modeling times between different computational models for case 2.

Case 2	The model used by Wang and Wang [14]	The model developed in this study
Computational resources	9 nodes of 1.4 GHz AMD Athelon Thunderbird CPU and 512 MB DDR SDRAM	2.39 GHz Dual Core AMD Opteron CPU and 3.5 GB DDR SDRAM
Modeling time	Nearly 5 h for only one *IV* point	Nearly 4 h for a polarization curve including 18 *IV* points

Table 3
Comparisons of computational resources and modeling times between different computational models for case 3.

Case 3	The model used by Wang and Wang [15]	The model developed in this study
Computational resources	32 nodes of 2.8 GHz Intel Pentium 4 CPU and 1.0 GB DDR SDRAM	2.39 GHz Dual Core AMD Opteron CPU and 3.5 GB DDR SDRAM
Modeling time	Nearly 20 h for only one *IV* point	Nearly 1 and 2 h for a polarization curve including 18 *IV* points of case 3(a) and case 3(b), respectively

that when current densities increase, the $\bar{V}_{oc}^{C}$ of both cases 3(a) and 3(b) vary little, the values of which range between 1.190 V at 10 mA cm^{-2} and 1.184 V at 1500 mA cm^{-2} and between 1.193 V at 10 mA cm^{-2} and 1.186 V at 1500 mA cm^{-2}, respectively. However, with increasing current densities, $\bar{\eta}_C$, $\overline{\delta\phi_f}$ and $\overline{\delta\phi_s}$ all increase for cases 3(a) and 3(b). Comparing various polarization losses in Figs. 15 and 16, it is found that $\bar{\eta}_C$ increases from 0.158 V at 10 mA cm^{-2}–0.467 V at 1500 mA cm^{-2} for case 3(a) to 0.168 V at 10 mA cm^{-2}–0.479 V at 1500 mA cm^{-2} for case 3(b). $\overline{\delta\phi_f}$ decreases from 0.002 V at 10 mA cm^{-2}–0.168 V at 1500 mA cm^{-2} for case 3(a) to 0.001 V at 10 mA cm^{-2}–0.098 V at 1500 mA cm^{-2} for case 3(b). $\overline{\delta\phi_s}$ is the same for case 3(a) and case 3(b) with a value ranging between 5×10^{-4} V at 10 mA cm^{-2} and 0.068 V at 1500 mA cm^{-2}.

Based on the above descriptions, $\bar{\eta}_C$ is the primary polarization loss, $\overline{\delta\phi_f}$ is the secondary, and $\overline{\delta\phi_s}$ is the minimum. By observing further that performance differences between different cell temperatures are dominated by polarization loss, it can be determined that under the same current density, the overpotentials of case 3(a) are slightly higher than those in case 3(b), while the ionic-phase ohmic losses of case 3(a) are much lower than those of case 3(b). This leads to the finding that the total polarization losses of case 3(b) are smaller than for case 3(a) because of smaller ionic-phase ohmic losses caused by lower cell temperatures.

3.5. The comparisons of modeling ability between different computational models for cases 2 and 3

In order to compare the modeling ability of the computational models in this study to that of Wang and Wang [14,15], Tables 2 and 3 give computational resources and modeling times for cases 2 and 3, respectively. First, Table 2 tabulates that in case 2, Wang and Wang [14] takes nearly 5 h to implement a simulation for only one *IV* point on 9 nodes of a 1.4 GHz AMD Athelon Thunderbird CPU with 512 MB DDR SDRAM. This study takes almost 4 h to implement 18 simulations for the polarization curve, including 18 *IV* points on the HP xw9300 Workstation of one node of a 2.39 GHz Dual Core AMD Opteron CPU with 3.5 GB DDR SDRAM. Second, Table 3 tabulates that in case 3, Wang and Wang [15] takes nearly 20 h to implement a simulation for only one *IV* point on 32 nodes of a 2.8 GHz Intel Pentium 4 CPU with 1.0 GB DDR SDRAM. This study takes almost 1 and 2 h, respectively, to implement 18 simulations for the polarization curve, including 18 *IV* points of case 3(a) and case 3(b) on the same HP xw9300 Workstation.

Because this study adopts the models covered by one single oxidant channel as computational domains, case 3, with shorter total channel lengths, instead requires fewer computational grids relative to case 2, and this leads to case 3 requiring less modeling time than case 2. If comparing the computational models of this study to that of Wang and Wang [14,15], then this study can implement extensive modeling works in a more efficient manner by using fewer computational resources. This is because in this

study, a cathode physical model that only includes the regions covered by one oxidant channel is considered. Therefore, compared with CFD modeling with fuel-cell models including the regions covered by all channels, great simplification of computational models with this study can improve computational efficiency, especially for large-scale fuel-cell modeling. In addition, this model, which consists of one dimension along the direction of oxidant flow and one dimension along the z-direction, forms the main framework for developing the mathematical formulations. This leads to the fact that the number of governing equations and variables that need to be solved in this study are much less than those that are solved in three dimensions; hence, computational efficiency is promoted again. Therefore, combinations of simplified models and reduced dimensions are the key to the computational efficiency of this study, making it superior to traditional CFD modeling. This explains why extensive modeling work can be completed with fewer computational resources and in less time.

For original fuel-cell modeling that requires several hours to several tens of hours, this study presents refined and powerful computational models as a solution that can help researchers deal with this troublesome issue. This study can not only evaluate overall performance characteristics, such as polarization curves, output powers, reactant flow rates and pressure drops, but can also provide related property distributions to elucidate and explain microscopic phenomena and physical mechanisms within fuel cells. For the effect of property distributions on the cell performance of the aforementioned case 1, further analyses and discussions will be given in the second part of this series of studies.

4. Conclusions

This study presents the model development and validation of an efficient method of numerical predictions for the performance characteristics of fuel cells. In order to verify the accuracy and reliability of the computational models in this study, three cases were analyzed, and some key conclusions are summarized as follows:

1. From the comparisons between experimental and predicted polarization curves for case 1, the computational models in this study can predict cell performances under different operating conditions, both qualitatively and quantitatively. For cases 2 and 3, the computational models of this study can not only accurately reproduce the *IV* value and output power at a specific operating point, but can also quickly give predictions at other operating points to produce polarization curves and the corresponding powers.
2. In addition to the polarization curves and output powers, the computational models in this study can also predict overall performance characteristics, such as reactant flow rates and pressure drops, and various components of cell voltages. These modeling results can not only evaluate the effects of flow

designs, operating conditions or material parameters on cell performance, but can also provide the reactant flow rates and pressure drops necessary for fuel cells so that researchers can choose appropriate system components, such as air blowers. Computation of open-circuit voltages and various polarization losses help researchers identify major factors dominating cell performance, which can be further improved and promoted according to in-depth analyses of various components of cell voltages.

3. Compared with known simulations of large-scale fuel cells, the computational models of this study can complete extensive modeling works in a more efficient manner by using fewer computational resources. Therefore, for realistic engineering designs, this study presents a better solution, which can not only allow researchers to perform simulations of fuel cells at various scales with fewer computational resources but can also substantially decrease costs and the time necessary for fuel-cell experiments.

For theoretically fundamental investigations, the computational models of this study can also provide data or pictures of property distributions. Therefore, to further investigate the effects of different operating conditions on cell performance, the distributions of various components of cell voltages and related properties governing these components for case 1 will be given in the second part of this series of studies. To explain the interactions between various properties and physical mechanisms governing these phenomena, a systematical method is used in the second part to perform detailed and in-depth analyses.

Acknowledgement

References

[1] T.E. Springer, T.A. Zawodinski, S. Gottesfeld, J. Electrochem. Soc. 136 (1991) 2334.
[2] D.M. Bernardi, M.W. Verbrugge, J. Electrochem. Soc. 139 (1992) 2477.
[3] T.V. Nguyen, R.E. White, J. Electrochem. Soc. 140 (1993) 2178.
[4] V. Gurau, H. Liu, S. Kakac, AICHE J. 44 (1998) 2410.
[5] S. Um, C.Y. Wang, K.S. Chen, J. Electrochem. Soc. 147 (2000) 4485.
[6] W. He, J.S. Yi, T.V. Nguyen, AICHE J. 46 (2000) 2053.
[7] Z.H. Wang, C.Y. Wang, K.S. Chen, J. Power Sources 94 (2001) 40.
[8] C.Y. Wang, P. Cheng, Int. J. Heat Transfer 39 (1996) 3607.
[9] S. Mazumder, J.V. Cole, J. Electrochem. Soc. 150 (2003) A1503.
[10] S. Mazumder, J.V. Cole, J. Electrochem. Soc. 150 (2003) A1510.
[11] M. Hu, A. Gu, M. Wang, X. Zhu, L. Yu, Energy Convers. Manage. 45 (2004) 1861.
[12] M. Hu, X. Zhu, M. Wang, A. Gu, L. Yu, Energy Convers. Manage. 45 (2004) 1883.
[13] H. Meng, C.Y. Wang, Chem. Eng. Sci. 59 (2004) 3331.
[14] Y. Wang, C.Y. Wang, J. Power Sources 147 (2005) 148.
[15] Y. Wang, C.Y. Wang, J. Power Sources 153 (2006) 130.
[16] G. Inoue, Y. Matsukuma, M. Minemoto, J. Power Sources 157 (2006) 153.
[17] G. Inoue, T. Yoshimoto, Y. Matsukuma, M. Minemoto, H. Itoh, S. Tsurumaki, J. Power Sources 162 (2006) 81.
[18] G. Inoue, T. Yoshimoto, Y. Matsukuma, M. Minemoto, H. Itoh, S. Tsurumaki, J. Power Sources 162 (2006) 94.
[19] X.D. Wang, Y.Y. Duan, W.M. Yan, J. Power Sources 172 (2007) 265.
[20] J.K. Kuo, T.H. Yen, C.K. Chen, J. Power Sources 177 (2008) 96.
[21] C.H. Min, J. Power Sources 186 (2009) 370.
[22] J. Lobato, P. Canizares, M.A. Rodrigo, F.J. Pinar, E. Mena, D. Ubeda, Int. J. Hydrogen Energy 35 (2010) 5510.
[23] P.C. Sui, S. Kumar, N. Djilali, J. Power Sources 180 (2008) 410.
[24] H. Ly, E. Birgersson, M. Vynnycky, A.P. Sasmito, J. Electrochem. Soc. 156 (2009) B1156.
[25] G.S. Kim, P.C. Sui, A.A. Shah, N. Djilali, J. Power Sources 195 (2010) 3240.
[26] W. Yuan, Y. Tang, M. Pan, Z. Li, B. Tang, Renew. Energy 35 (2010) 656.
[27] K. Jiao, X. Li, Int. J. Hydrogen Energy 35 (2010) 5077.
[28] N. Khajeh-Hosseini-Dalasm, K. Fushinobu, K. Okazaki, Int. J. Hydrogen Energy 35 (2010) 4234.
[29] G. Dagan, Flow and Transport in Porous Formations, Springer-Verlag, 1989.
[30] R.B. Bird, W.E. Stewart, E.N. Lightfoot, Transport Phenomena, Wiley, 2002.
[31] F. Barbir, PEM Fuel Cells: Theory and Practice, Elsevier, 2005.
[32] C.Y. Wang, C. Beckermann, Int. J. Heat Mass Transfer 36 (1993) 2747.
[33] C.Y. Wang, Numer. Heat Transfer B: Fundam. 31 (1997) 85.
[34] R.W. Fox, A.T. McDonald, Introduction to Fluid Mechanics, Wiley, 1994.
[35] U. Pasaogullari, C.Y. Wang, J. Electrochem. Soc. 151 (2004) A399.
[36] E.A. Ticianelli, C.R. Derouin, S. Srinivasan, J. Electroanal. Chem. 251 (1988) 275.